CHALMERS
UNIVERSITY OF TECHNOLOGY

Spectroscopic Investigation of Novel CARDIPY Derivatives

Steady-state and time-resolved characterization of a new class of fluorophores

Thesis in Materials Chemistry

JESSICA ELIZABETH BAIR

DEPARTMENT OF CHEMISTRY AND CHEMICAL ENGINEERING
CHALMERS UNIVERSITY OF TECHNOLOGY
Gothenburg, Sweden 2024
www.chalmers.se

Degree project report 2024

Spectroscopic Investigation of Novel CARDIPY Derivatives

Steady-state and time-resolved characterization of a new class of fluorophores

JESSICA ELIZABETH BAIR

CHALMERS
UNIVERSITY OF TECHNOLOGY

Department of Chemistry and Chemical Engineering
Chalmers University of Technology
Gothenburg, Sweden 2024

Spectroscopic Investigation of Novel CARDIPY Derivatives
Steady-state and time-resolved characterization of a new class of fluorophores
JESSICA ELIZABETH BAIR

Supervisor: Carlos Benitez-Martin, Joakim Andreasson
Examiner: Joakim Andreasson, Department of Chemistry and Biochemistry, Chemistry and Chemical Engineering

Degree project report 2024
Department of Chemistry and Chemical Engineering
Chalmers University of Technology
SE-412 96 Gothenburg
Sweden
Telephone +46 31 772 1000

Cover: Fluorescence of CARDIPYs **2a-f** in aqueous solution.

Typeset in LaTeX
Gothenburg, Sweden 2024

Spectroscopic Investigation of Novel CARDIPY Derivatives
Steady-state and time-resolved characterization of a new class of fluorophores
JESSICA ELIZABETH BAIR
Department of Chemistry and Chemical Engineering
Chalmers University of Technology

Abstract

A set of newly-synthesized hydrophilic carbon-dipyrromethene (CARDIPY) derivatives have undergone photophysical characterization within a series of solvents. Discussed optical properties include steady-state absorption and emission maxima, fluorescence quantum yields, and fluorescence lifetimes. The influence on these properties from backbone substitution patterns, solvent polarity, and modification at the *meso*-position are explored. Due to steric hindrance and rigidity effects, fluorescence quantum yield as well as fluorescence lifetimes are generally observed to increase with added backbone substituents. In parallel, a slight negative solvatochromic effect was observed in the absorption and emission energies of all the compounds. In most cases, this resulted in an increased fluorescence quantum yield with decreasing polarity. However, fluorescence quantum yield is also thought to be affected by emissive aggregates, which could be detected in the fluorescence lifetime measurements. The decay patterns of most of the compounds consist of a short-lived monomer component, and a long-lived aggregation component. Monoexponential decay patterns were observed in the CARDIPYs without auxiliary groups that exhibit intramolecular rotation.

Keywords: CARDIPY, fluorescence, photophysics, spectroscopy, water-soluble dyes.

Acknowledgements

First, I would like to give a huge thank you to my mentor, Carlos Benitez-Martin, for providing me with the TDDFT calculations along with his interpretation of the results. Had it not been for this, along with his continuous scientific guidance and emotional support, I would not have made it even halfway through this project. I would also like to thank my supervisor, professor Joakim Andréasson, for the warm welcome into his research group, as well as his guidance. My work with him over this past year has been more than delightful. Finally, I would like to mention that this work would not have been possible if not for the CARDIPYs developed and provided by Cassandra Fleming and Mark Johnson at Auckland University of Technology.

Jessica Elizabeth Bair, Gothenburg, May 2024

List of Acronyms

Below is the list of acronyms that have been used throughout this report listed in alphabetical order:

ACN	Acetonitrile
BODIPY	**Bo**ron-**Dipy**rromethene
CARDIPY	**Car**bon-**Dipy**rromethene
DCM	Dichloromethane
DFT	Density-Functional Theory
FMO	Frontier Molecular Orbital
HOMO	Highest Occupied Molecular Orbital
LUMO	Lowest Unoccupied Molecular Orbital
NaOH	Sodium Hydroxide
TDDFT	Time-Dependent Density-Functional Theory
UV	Ultraviolet
UV-Vis	Ultraviolet-Visible

Contents

List of Figures

List of Tables

1

Introduction

1.1 Background

Over the past few decades, exploiting the phenomenon of fluorescence has led to the development of technology within a wide range of disciplines. Methods in fluorescence spectroscopy have applications in fields spanning from optoelectronics to medical diagnostics and therapeutics[1]. In regards to biochemical measurements, methods requiring the use of radioactive tracers are falling out of favor to fluorescence detection methods, which can achieve high sensitivity without the high material costs or handling complications[2]. Fluorescence imaging is often chosen in diagnostics for its ability to maintain these benefits while minimizing invasiveness[3]. The unique photophysical properties of fluorophores, which are compounds that show detectable fluorescence, are fundamental to a number of fluorescence monitoring methods[4]. Steady-state properties, interconnected with properties found in the time-resolved regime, form the basis for methods in quantitative analysis[5] and microscopy[6], as well as experiments in fluorescence anisotropy[7], energy transfer[8], and quenching[9].

Fluorophores can be classified in relation to their natural occurrence in biomolecules. Intrinsic fluorophores are found naturally in a biological structure: these include many enzyme cofactors such as NADH (reduced nicotinamide adenine dinucleotide), pyridoxyl phosphate, and riboflavin, as well as the aromatic amino acids tryptophan, tyrosine, and phenylalanine[2]. A great deal of autofluorescence in cells originates from proteins with bound NADH[10], and endogenous proteins with prosthetic riboflavin derivatives (flavoproteins)[11]. NADH has an absorption maximum around 340 nm and emits around 450 nm, while flavins excite at around 360 nm and emit near 520 nm[12]. Aside from enzyme cofactor-derived fluorescence, tissues with proteins rich in the aromatic amino acids, such as dermal collagen, will display emission behaviors representing all the emitting species available in the structure[2]. Many molecules and structures of interest, however, display either inadequate fluorescence relative to the experiment, or none at all. In biological samples, the emission behaviors of intrinsic fluorophores become more complex when accounting for structural effects. For proteins like collagen, fluorescence spectra involve several overlapping bands, reported not only belonging to tyrosine, but also its interactions, such as dityrosine (two neighboring tyrosines), aggregated species, and even other fluorophores like glycation adducts[13].

Arising from the complications related to lack of control of the structures being monitored is the need for extrinsic fluorophores. These are added to a sample to give an analyte the desired fluorescent behaviors for an experiment[2]. There are many types of extrinsic fluorophores that can act as labels, dyes, or probes. Some examples include organic dyes, metal-ligand complexes, fluorescent polymers, and nanoparticles[4]. The fluorescein and rhodamine families are two groups of very commonly-used labels due to their benefits in biological samples. The absorption (λ_{abs}) and emission (λ_{em}) maxima of many derivatives lie towards the lower energies of the visible region[14]. This, combined with their high fluorescence quantum yields (Φ_F), can minimize the issues arising from undesired background fluorescence[2]. The Fluorescein parent and the rhodamine 6G derivative, shown in Figure 1.1 are two of the most well-established standards used to estimate the fluorescence quantum yields of other fluorophores[15]. The limitations associated with these groups is the small Stokes shifts bridging their broad absorption and emission bands, which can lead to overlap when multiple emissive species are present.

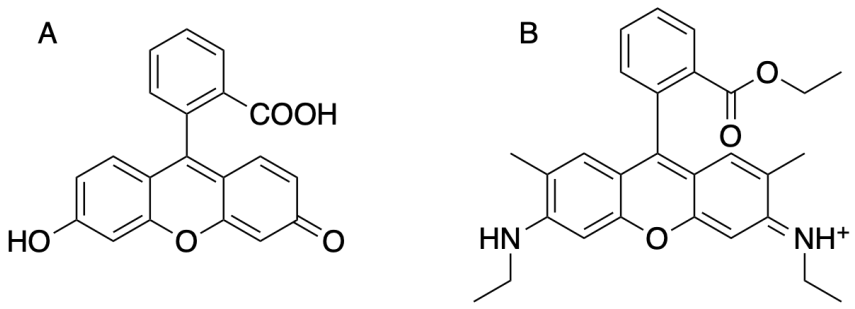

Figure 1.1: Structures of Fluorescein (A) and rhodamine 6G (B).

Boron-dipyrromethene (BODIPY) derivatives were introduced in 1968, and serve as another common group of labels these days. Like the fluorescein and rhodamine families, their absorption and emission wavelengths can easily be tuned with slight chemical variations[16]. In spite of having even smaller Stokes shifts, their emission spectra tend to be more narrow than those of the fluoresceins and rhodamines, allowing for better differentiation between emissive species. Even higher fluorescence quantum yields are possible in some of the brighter compounds[2]. In the context of bioimaging, a common complication associated with BODIPYs is their lipophilic nature and tendency to form nonemissive aggregates at low concentrations in aqueous solutions[17]. Many derivatives are not commercially available and must be designed specifically for their applications, involving time-demanding and expensive synthetic procedures[18][19].

As an alternative to the BODIPYs, a new class of carbon-dipyrromethene (CARDIPY) derivatives has recently been developed. With a simple replacement of the boron atom for a carbon, their structures are analogous to the BODIPYs, and thus employ similar nomenclature systems (Figure 1.2). Because of the overall cationic character arising from this replacement, CARDIPY derivatives show high water-solubility, raising their appeal for biological applications[20]. However, at this point, only a handful of reports have made any mention of synthesizing such compounds.

The first report of CARDIPYs came up in 1991, where Koek *et al.* synthesized two derivatives emitting green light with high fluorescence quantum yields (Φ_F = 0,28 and 0,40)[21]. Here, their family had not yet been named, and they were instead referred to as *E-anti* and *Z-syn* pyrromethenium salts. In 2020, Guo *et al.* introduced the term CARDIPY in their report of fifteen newly-synthesized, water-soluble derivatives with tunable fluorescent properties from the visible to near-infrared regions[20]. In 2023, Ng *et al.* successfully demonstrated the use of a tetrazine-caged CARDIPY derivative as a fluorescent probe in the imaging of human glioblastoma cells[22].

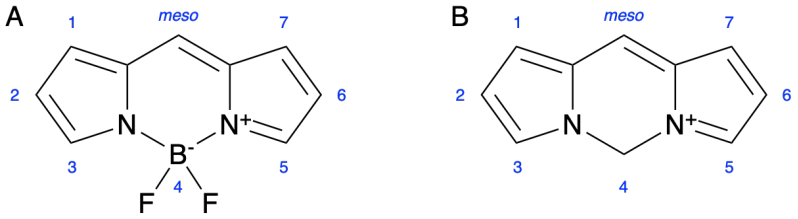

Figure 1.2: Backbone structures and nomenclature system of BODIPY (A) and CARDIPY (B).

1.2 Purpose

The few current studies have certainly showed great potential for the CARDIPY family, emphasizing a focus in cancer treatments as well as other mitochondria-targeting photodynamic therapy. As compared to the BODIPYs, these compounds display great cell-membrane penetration, and mitochondria accumulation[20]. Synthesis of more water-soluble derivatives, along with their photophysical characterization and applications studies would give many more options and further advance the field.

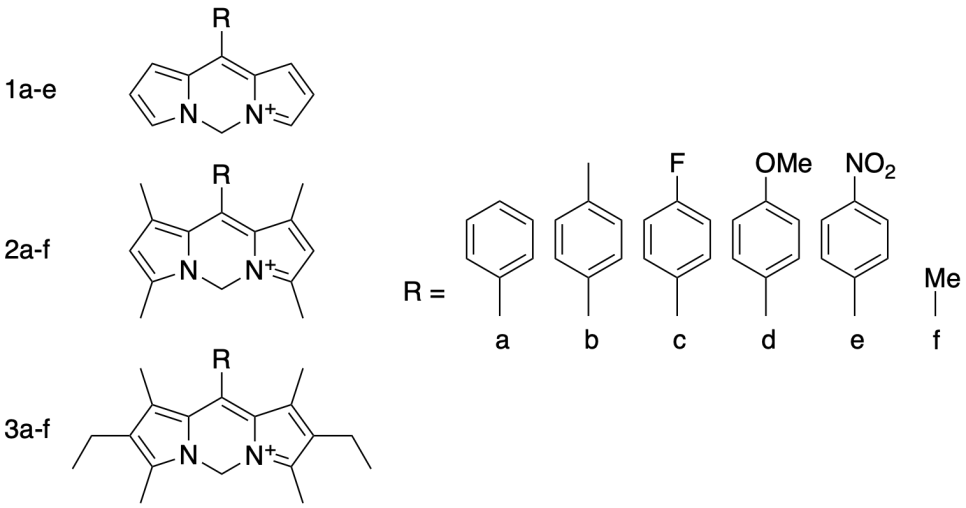

Figure 1.3: Naming system of all the CARDIPY derivatives assigned for spectroscopic characterization in this work. Numbers 1, 2, and 3 refer to scaffolding options, and *meso*-position substitutions are represented by a-f (a-e for series 1).

In this work, we present the photophysical properties of a set of new CARDIPY derivatives with possible applications within the above mentioned fields (shown in Figure 1.3), synthesized by our collaborators Cassandra Fleming and Mark Johnson at Auckland University of Technology via their improved synthetic methodology.

1.3 Goals

The goals for this research involve the photophysical characterization of the presented CARDIPY derivatives within both the steady state and the time-resolved regime. The relevant properties include absorption, excitation, and emission maxima, and fluorescence quantum yields and lifetimes within the realm of multiple solvents. Results will be shown in a way that highlights the patterns arising from modifying the CARDIPY backbone, the substitution at the *meso*-position, and the effect of solvent. Discussion will involve the potential applications of the compounds within the field of bioimaging, as well as suggestions of future CARDIPY derivatives to further explore structure-property relationships.

2

Theory

2.1 Fluorescence

The field of spectroscopy revolves around light-matter interactions and their associated processes. Those relevant to this work are depicted in Figure 2.1. Absorption, depicted by blue arrows, is a transition from a lower to a higher electronic state, which occurs as the result of an interaction between light and the electronic states of a system. This process is governed within the "ultrafast" regime, occurring in around 10^{-15} seconds[2]. According to the Franck-Condon principle, the timescale of this process allows absorption to take place before significant nuclei displacement. Because of this, the system is often excited to some vibrational excited state within an electronic excited state. Following absorption, the system quickly dissipates the excess energy and relaxes to the lowest vibrational state within the lowest excited singlet electronic state, S_1. Depending on the initial state after photoexcitation, the pathway to S_1 consists of some combination of nonradiative relaxation steps. Internal conversion (dotted arrows) is an energy transfer to a lower electronic state, occurring in the range of 10^{-11} to 10^{-9} seconds. Vibrational relaxation (dashed arrows) occurs within the same electronic energy level, and is often even faster than internal conversion (10^{-12} to 10^{-10} seconds). Due to the quick rates of these nonradiative steps, fluorescence, which is much slower, generally occurs from the lowest vibrational state within S_1. This is commonly known as Kasha's rule[2]. Fluorescence, depicted by green arrows, is a transition characterized by the return of the molecule to the ground electronic state (S_0) without experiencing a change in spin state. The lifetimes associated with fluorescence usually last between 10^{-9} and 10^{-8} seconds. Another luminescence behavior is phosphorescence, depicted by orange arrows. This is the emission of a photon from a molecule in the triplet excited state, T_1. The transition from S_1 to T_1 is known as intersystem crossing, and occurs between 10^{-10} and 10^{-8} seconds. Phosphorescence emission is also governed by Kasha's rule, occurring from the lowest vibrational state in T_1. Because of the "forbidden" transition from the triplet excited state to the ground state, and the resulting low emission rates (10^{-3} to 10^{0} s^{-1}), phosphorescence can be observed for milliseconds to seconds, and in some cases even several minutes[2]. Phosphorescence is not often a valid pathway in room-temperature liquids due to competition with non-radiative decay and quenching processes such as collisional and static quenching[2], so in these cases fluorescence is much more likely to be observed.

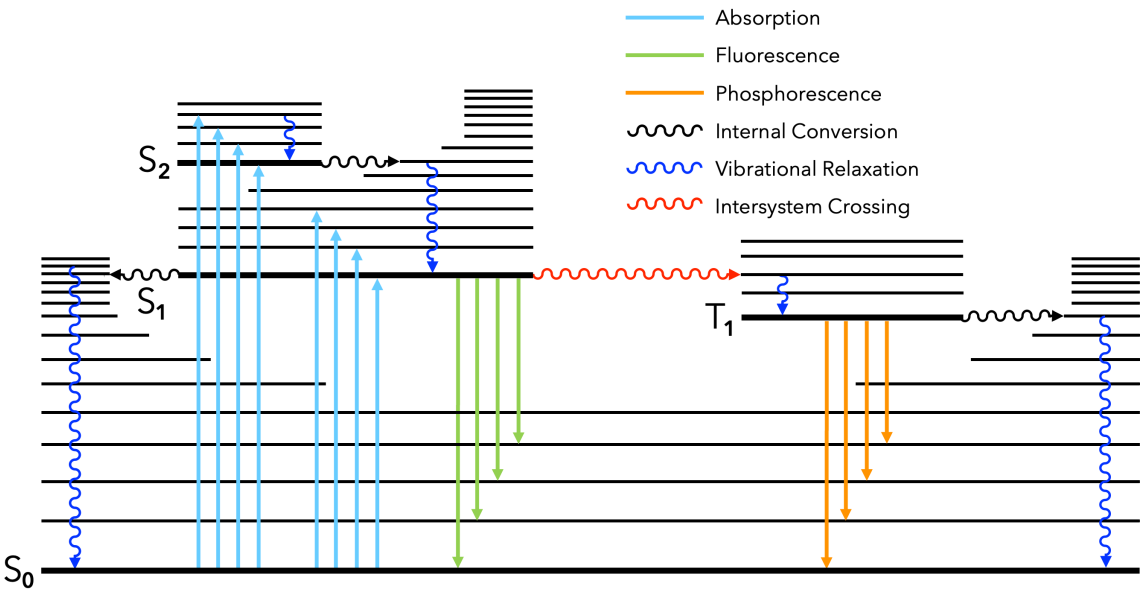

Figure 2.1: A simple Jablonski diagram illustrating various transitions between electronic states.

After a molecule relaxes to the lowest vibrational state within S_1, the behaviors that can follow are in competition with one another. Because of the nonradiative processes participating in deactivation, fluorescence is rarely quantitative. Fluorophores are compounds for which there is a detectable level of fluorescence emission. With regards to organic compounds, fluorescence is typical in molecules with π-conjugated systems, which can include planar aromatic molecules. The CARDIPYs in this work have conjugation around their backbones, and assume a nearly-planar conformation, allowing observable fluorescence.

2.2 Fundamental equations

The efficiency of the fluorescence emissive pathway is quantified by the fluorescence quantum yield, which represents the ratio of photons emitted by fluorescence to the total number of photons absorbed by the system. The fluorescence quantum yield approaches unity when this ratio is increased. Deviations from unity occur upon the introduction of nonradiative processes that can lead to deactivation.

To experimentally determine a fluorescence quantum yield, absolute and comparative methods can be used. The determination of fluorescence quantum yields via absolute methods requires rather sophisticated and delicate technology, for instance, an integrating sphere. These setups have been developed to eliminate complications arising from variables that can differ due to scattering in samples, such as polarization and refraction index of solvents[23]. The available setup that can determine fluorescence quantum yield is quite limited to solid-state samples, as there is a high risk of damage when solutions are involved. This is not detrimental to this project, as the fluorescence quantum yield can be estimated just as well via comparative methods. Better suited for the purposes of this report, the relative method may be

used to estimate the fluorescence quantum yield of a sample through a comparison to a reference. Used in this work, Equation 2.1 represents the fluorescence quantum yield of the sample (Φ_F) as a ratio of experimental absorption and emission data acting on Φ_f^s, the fluorescence quantum yield of the reference.

$$\Phi_F = \frac{F^i f_s n_i^2}{F^s f_i n_s^2} \Phi_f^s \tag{2.1}$$

F^i and F^s are the integrated intensities of the sample and reference emission spectra, and n_i and n_s are the refractive indices of the sample and reference. Because the fluorophores are measured at such low concentration, the refractive indices can be approximated by those of the solvents alone. The variables f_i and f_s are the absorption factors (fraction of light absorbed) of the sample and reference, representing the number of photons absorbed at the excitation wavelength. Absorption factors can be calculated using Equation 2.2, where A_x is the absorption of either the sample or reference at the excitation wavelength.

$$f_x = 1 - 10^{-A_x} \tag{2.2}$$

The fluorescence lifetime (τ_F) represents the average time the molecule spends before emitting a photon from the S_1 state. In the context of this work, it is extracted from a mathematical fit to the decay measurement. The fluorescence lifetime and the fluorescence quantum yield are represented by the rate constants of the associated radiative (k_F) and non-radiative (k_{nr}) processes, shown in Equations 2.3 and 2.4.

$$\Phi_F = \frac{k_F}{k_F + k_{nr}} \tag{2.3}$$

$$\tau_F = \frac{1}{k_F + k_{nr}} \tag{2.4}$$

Finally, Equation 2.5 expresses the radiative rate constant as a simple relation between the fluorescence quantum yield and the fluorescence lifetime. This expression is derived through a combination of Equations 2.3 and 2.4.

$$k_F = \frac{\Phi_F}{\tau_F} \tag{2.5}$$

3

Experimental Techniques

3.1 Steady-State Ultraviolet-Visible Spectroscopy

Steady-state ultraviolet-visible (UV-Vis) spectroscopy is a technique used to record a sample's transmittance or absorption at certain wavelengths within the ultraviolet and visible light spectrum. The spectra obtained from the ultraviolet (UV) and visible regions are often used for photophysical characterization and sample preparation. According to Beer-Lambert law (Equation 3.1), under low concentration regimes, absorption is proportional to molar absorptivity (ε), sample path length (d), and analyte concentration (c). When intermolecular interactions do not affect this relationship with concentration, UV-Vis measurements may be used for quantitative analysis. Absorption at a single wavelength is often recorded over time intervals such that the kinetics of a physical or chemical reaction may be traced.

$$A = \varepsilon dc \tag{3.1}$$

$$A = -log(I/I_0) \tag{3.2}$$

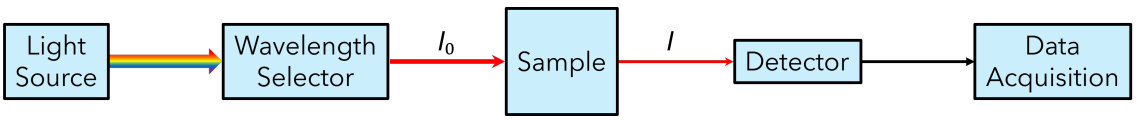

Figure 3.1: Schematic for a simple steady-state UV-Vis spectrophotometer.

UV-Vis instruments use an elementary setup that allows the direct comparison of the light intensity before and after passing through a sample. The ability for light at certain wavelengths to pass through is known as transmittance, which is related to absorption through a negative logarithmic function (Equation 3.2). Because measurements depend on this comparative relationship, data readout is given in a unitless dimension.

3.2 Steady-State Fluorescence Spectroscopy

Steady-state fluorescence spectroscopy, or fluorimetry, utilizes the phenomenon of fluorescence to record the intensity of light emitted by a sample. Like with steady-state UV-Vis, fluorescence spectroscopy may be used for characterization, and quan-

titative analysis. A fluorescence spectrophotometer may be used to record fluorescence spectra in emission mode (constant excitation wavelength, varied detection wavelength), or in excitation mode (varied excitation wavelength, constant detection wavelength). Excitation spectra share similarities with absorption spectra, but deviate depending on the non-emissive chromophores present in the sample. Emission spectra typically follow a mirror-image rule to the absorption spectrum, but as a result of Kasha's rule will not reflect transitions to higher-lying excited states. Deviations from the mirror image rule are observed when subsequent processes take place after excitation, for example, intramolecular charge transfer[2].

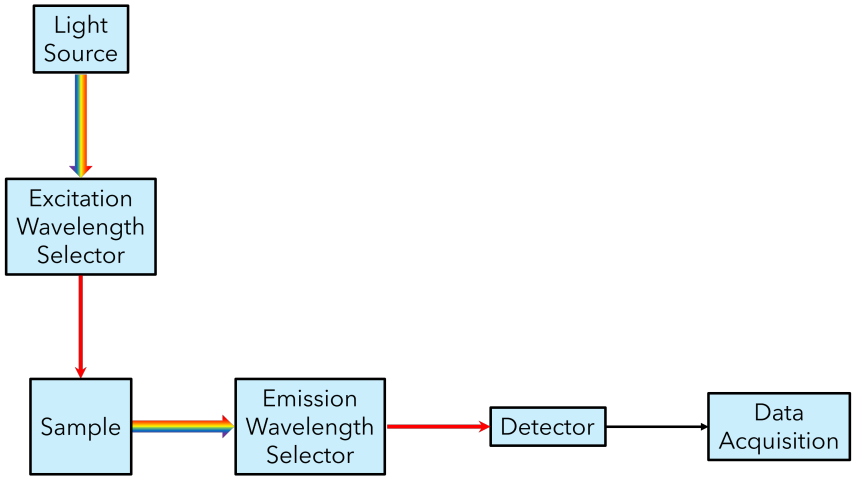

Figure 3.2: Schematic for a simple steady-state emission spectrophotometer.

To avoid overlap with the excitation light, a simple fluorimeter typically detects emission from the sample from an angle orthogonal to the source. Readout is given in the unit of fluorescence intensity. The intensity read by the detector at a certain wavelength can be tuned by changing the excitation wavelength, or by changing the slit widths of the excitation and emission wavelength selectors. Similar to absorption, fluorescence intensity shares a proportional relationship with concentration. This applies at low concentration conditions, or in the absence of phenomena affecting the emissive properties of a compound, such as aggregation.

3.3 Time-Resolved Emission Spectroscopy

Unlike in the steady-state, where a signal is averaged over time, time-resolved fluorescence spectroscopy collects fluorescence signal as a function of time after excitation by a pump of light. Time-resolved measurements are read out as a collection of emission signals at a certain wavelength. Lifetimes are determined through the fit of a mathematical expression, for example an exponential decay function (Equation 3.3), to the collection of data. In the absence of self quenching in high concentration regimes, fluorescence lifetimes do not have a direct relationship with concentration. However, they do depend on the interactions between fluorophore molecules and their environments.

$$I(t) = I_0 \cdot [A \cdot e^{-t/\tau_F}] \tag{3.3}$$

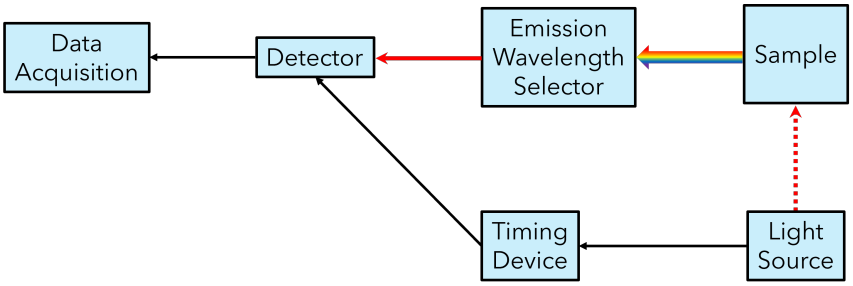

Figure 3.3: Schematic for a simple time-resolved emission spectrophotometer.

3.4 Experimental Details

All fluorophores presented in Results were prepared in ultrapure water (resistivity 18,2 MΩ.cm at 25 °C), dichloromethane (99,8%, spectroscopic grade, Thermo Fischer), and acetonitrile (≥99.9%, spectroscopic grade, Merck) via optical dilution to $0,05 < Abs_{max} < 0,15$.

Absorption spectra used for optical characterization were recorded using an Agilent Cary 3500 UV-Visible Multicell Peltier. Measurements were taken using a scan rate of 1000 nm/min with a spectral bandwidth of 2,00 nm, and controlled at 21,0 °C with variance of ± 0,1 °C. Absorption spectra for kinetic traces were recorded using a Varian Cary 50 Bio UV-Visible Spectrophotometer on scanning kinetics mode over a total of 24 hours in 30-minute cycles.

Emission and excitation spectra reported here were collected using a Spex Detec R928 with integration time of 1 s. Fluorescence quantum yields were calculated using the reference fluorophore method[15] (Fluorescein in 0,1 M sodium hydroxide (NaOH) solution, $\Phi_F = 0,925$[24]).

Fluorescence decays were recorded using a Lifespec picosecond-resolved diode laser. All samples were excited using a diode at 483 nm. Fluorescence detection was adjusted to the characteristic emission maximum of each compound, using a slit width of $\Delta\lambda = 4$ nm. In each measurement, 10000 counts were taken in the peak channel over a total of 2048 channels.

Fluorescence lifetimes were determined using exponential reconvolution fitting in the F900 data acquisition software. All spectra and fluorescence quantum yields presented here were worked up using the OriginPro software package (2023b).

4

Results and Discussion

4.1 General Properties

Absorption spectra for the CARDIPYs show a prevailing $S_0 \rightarrow S_1$ peak lying in the visible region ($486 \leq \lambda_{max} \leq 520$ nm), with a blue-shifted shoulder representing an apparent vibronic structure (Figure 4.1). Closer to the UV region, there is a broad band of low-intensity absorption. To gain insight on the absorption profiles, time-dependent density-functional theory (TDDFT) calculations were performed by postdoctoral researcher Carlos Benitez-Martin. It was observed in the calculated absorption spectra (Figure 4.2) that the absorption in this region contains contribution from several overlapping minor peaks representing transitions to higher lying excited states. Also consistent with the calculations, the absorption in this region is more pronounced in the absence of backbone substituents (compounds **1a** through **1e**). The emission spectra for **2a** and **3a** reflect the $S_0 \rightarrow S_1$ absorption peak and its shoulder well. **1a-e** are broad in their emission spectra towards the lower energies, a consequence of the unique twisting angle of each individual molecule[17]. The Stokes shifts tend to be quite small for most of the compounds.

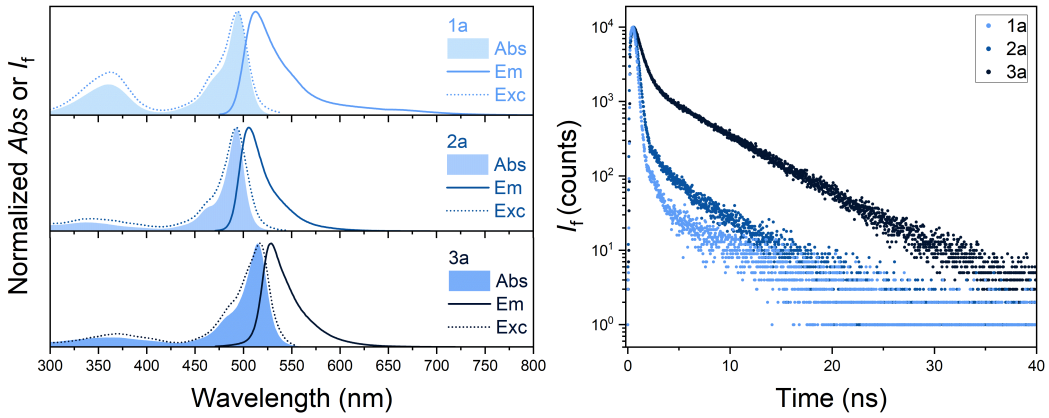

Figure 4.1: Steady-state spectra (left) and fluorescence decays (right) of **1a**, **2a**, and **3a** in aqueous solution.

Lifetime measurements for the most part fit well to a biexponential decay consisting of a sub-nanosecond component, and a component lasting several nanoseconds. From the fit, it is tempting to assume that the rotational junction bridging the π-electron density gives way to two emission pathways. However, aggregation offers a

better explanation for this phenomenon. In molecules with extended π-density that can distort out of plane, it has been established that restricting the torsion reduces nonemissive pathways, increasing the likelihood of emission. This can be achieved by adding steric hindrance and structural rigidity at the intramolecular level, or by adding friction from the microenvironment surrounding the molecule. In many compounds, emissive aggregates form that are able to hinder the torsion, increasing the fluorescence quantum yield. The emission from the aggregates, which are able to stay in the excited state for a longer amount of time, is discernible from emission from the monomers, whose time in the excited state is short-lived.

Inspired by previous work with BODIPYs[25], we believe the amplitude of the long-lived component in the decay can vary, depending on the nature of each compound's aggregates. High contribution from the long-lived component indicates more emission from the aggregates, disproportionately affecting the fluorescence quantum yield. Aggregation was observed in most of the samples at optically dilute concentrations. Accounting for the instrumental uncertainties associated with the steady-state recordings, the samples were not diluted below $Abs_{max} = 0,05$. Throughout this work, complications from aggregation were practically unavoidable.

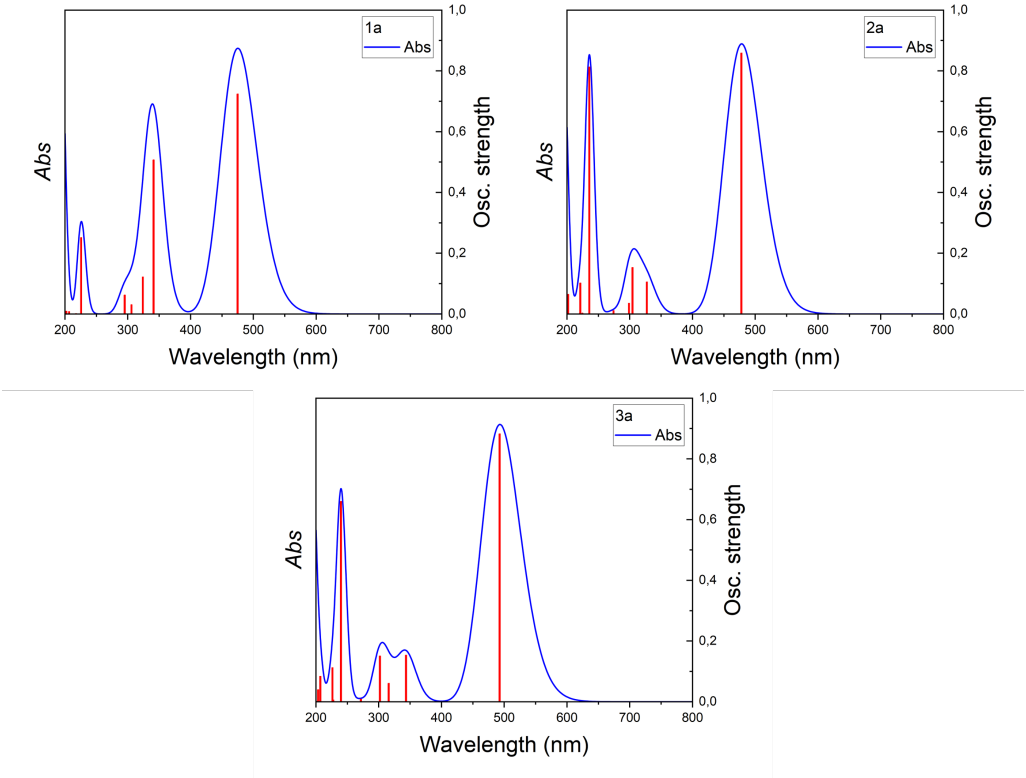

Figure 4.2: Calculated absorption spectra for **1a**, **2a**, and **3a**.

4.1.1 Substitution to the Backbone

Alkyl-substitution on the CARDIPY core has an effect on the absorption and emission maxima. As seen in Figure 4.3, the absorption and emission maxima of **3a** are

distinguished by an obvious red shift from those of **1a** and **2a**. Another observation is that the emission maximum of **1a** is red-shifted from that of **2a**, but the absorption spectra are quite similar. It may be tempting to assume that the absorption maximum of **1a** is similarly red-shifted from **2a**, but this difference falls within the instrumental uncertainty.

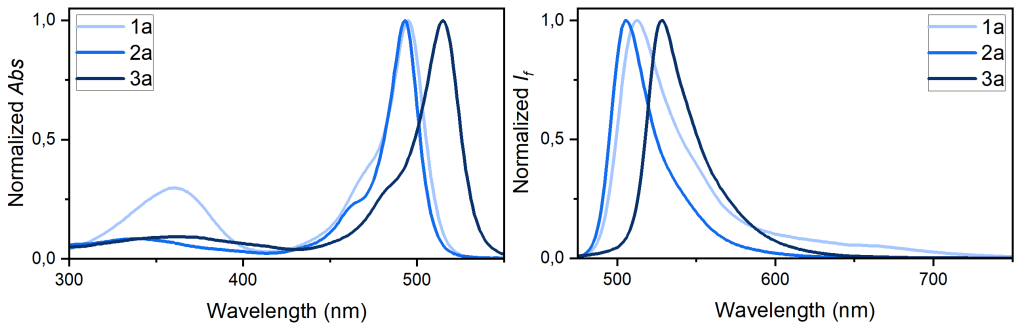

Figure 4.3: Stacked absorption (left) and emission (right) spectra of **1a**, **2a**, and **3a** to visualize the effect of the substitution pattern on λ_{abs} and λ_{em}.

Time-dependent density functional theory (TDDFT) calculations offer some insight on the effects of backbone substitution. Shown in Table 4.1, the calculated absorption and emission energies clearly reflect the overall red-shifted bands of **3a**. This effect can be explained through the analysis of the calculated frontier molecular orbitals (FMOs), shown in Figure 4.4. It is evident from the highest occupied molecular orbital (HOMO) that the added ethyl groups contribute to the π-conjugation, but its lowest unoccupied molecular orbital (LUMO) looks similar to that of **2a**. Experimentally-observed trends between **1a** and **2a** are also in part supported by the calculations. The similarities in their absorption spectra are well-reflected in the calculated absorption energies, as well as their corresponding HOMOs. However, the red shift in the experimental emission maximum of **1a** is not predicted by the calculated emission energies. In general, there are limitations associated with TDDFT, particularly pronounced for the calculation of trends in emission energies. However, the agreement between the calculations and the experimental data is still acceptable to the chosen level of theory, with deviations far below its typical error of 0,25 eV.

Table 4.1: Experimental data for **1a**, **2a**, and **3a** in water compared to photophysical data calculated at the SMD(water)/M062X/Def2TZVPP level of theory. Oscillator strength represented by f.

	Absorption				Emission			
Cpd.	f	Dominant Cpt.	E_{calc} [eV]	E_{exp} [eV]	f	Dominant Cpt.	E_{calc} [eV]	E_{exp} [eV]
1a	0,724	HOMO→LUMO	2,61	2,50	0,686	LUMO→HOMO	2,50	2,42
2a	0,859	HOMO→LUMO	2,59	2,51	0,807	LUMO→HOMO	2,45	2,45
3a	0,883	HOMO→LUMO	2,52	2,41	0,827	LUMO→HOMO	2,39	2,34

To understand the shift in the experimental emission maxima between **1a** and **2a**, one must consider the density functional theory (DFT) calculations in parallel with the results from TDDFT. DFT-optimized structures for **1a**, **2a**, and **3a** confirm steric hindrance in the presence of the methyl groups vicinial to the *meso*-position aromatic substituent (Figure 4.5). No major differences are seen in the planarity of **2a** and **3a**, whose aromatic substituents were optimized at a dihedral angle to the backbone by 76°and 75°, respectively. For **1a**, the lack of methyl groups results in a less perpendicular disposition of the phenyl group relative to the plane of the backbone, with a dihedral angle of 47°. As seen in the TDDFT calculations, this allows considerable displacement of electron density toward the aromatic substituent, specifically in the LUMO. The calculations are underestimating the extension of the π-conjugation, which may lend an explanation for the pronounced red shift in the emission maximum of **1a** from that of **2a**.

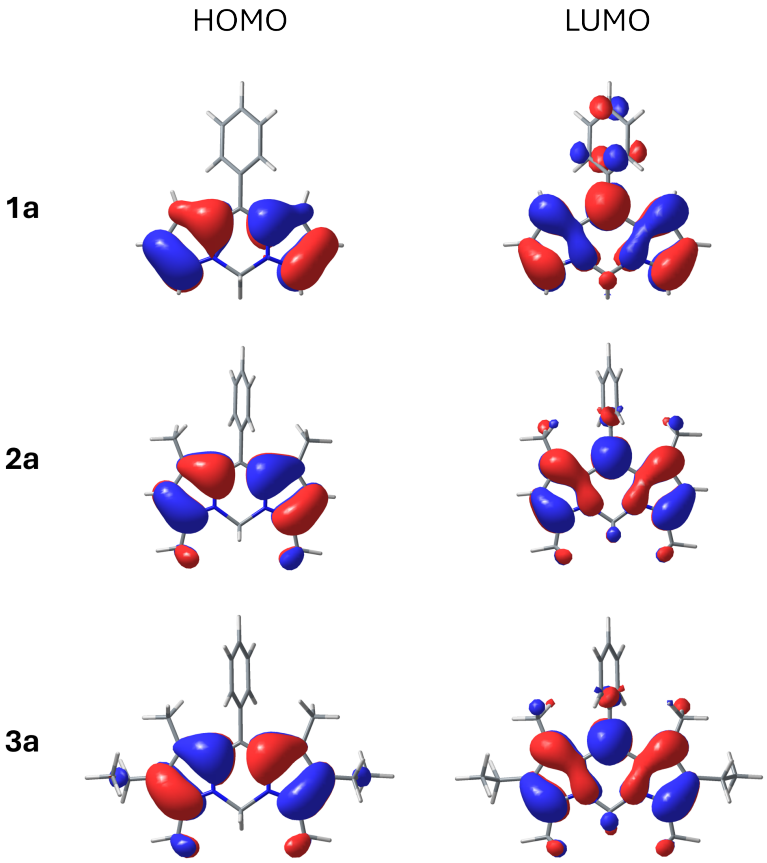

Figure 4.4: HOMO and LUMO orbitals for **1a**, **2a**, and **3a** calculated by TDDFT (SMD(water)/M062X/Def2TZVPP, isosurface: 0,03 e borh^{-3}).

The observations from the calculations are well-reproduced throughout the rest of the compounds, with many trends independent of the modification to the aromatic group at the *para*-position. In the DFT-optimized structures, the disposition of the aromatic group with increasing substitution density around the backbone systematically follows the trend of **1a**, **2a**, and **3a**. Experimentally, the influence from alkyl-substitution on the absorption and emission spectra remain consistent for most of

the compounds presented in this work. Similar effects have been reported by Loudet and Burgess with BODIPY dyes analogous to some of those in this report[26].

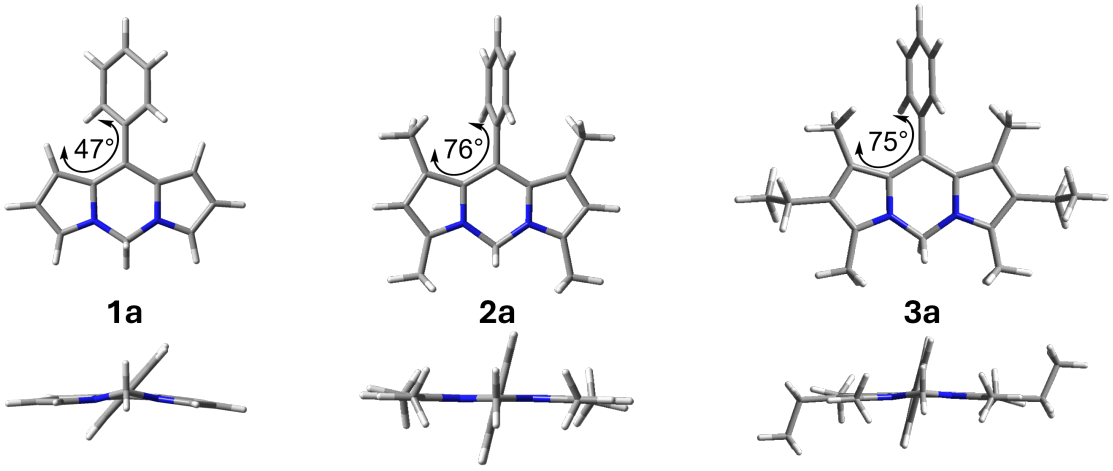

Figure 4.5: DFT-optimized structures of **1a**, **2a**, and **3a**. Calculated at the SMD(water)/M062X/Def2TZVPP level of theory. Dihedral angles along the π-conjugated system are indicated.

Fluorescence intensity tends to increase with crowding the CARDIPY core in compounds with *meso*-aromatic substituents. The presence of the methyl-groups directly adjacent to the phenyl ring expectedly increased the fluorescence quantum yield (Table 4.2). As reported in BODIPYs, adjacent steric hindrance inhibits the torsion of the aromatic group, decreasing the nonradiative deactivation experienced by the excited state[26]. An unexpected result was the systematic improvement the ethyl groups had on the fluorescence quantum yields. Their presence appears to increase rigidity, and in turn reduces the influence from nonradiative pathways. This is consistent with the increased duration of the short-lived component of the fluorescence decay in **3a**.

Table 4.2: Steady-state maxima, fluorescence quantum yields, and lifetime fit parameters of **1a**, **2a**, and **3a** in aqueous solution.

Cpd.	λ_{abs} [nm]	λ_{exc} [nm]	λ_{em} [nm]	Φ_F [%]	τ_1 [ns]	τ_2 [ns]	%$_1$	%$_2$	χ^2
1a	495	494	513	0,58	0,2	3,3	94	6,0	1,25
2a	493	493	506	4,6	0,3	3,8	86	14	1,04
3a	515	517	529	14	0,7	5,5	44	56	1,11

4.1.2 Solvatochromic Effect

Systematically, the CARDIPY absorption and emission bands experience a slight hypsochromic shift with an increase in solvent polarity. This effect is evident between the spectra in DCM and water (Figure 4.6). The difference between the aqueous spectra and those in ACN is more subtle, the shift falling within the error associated with the instrumentation. This behavior is indicative of a negative solvatochromic

effect, meaning the ground state is stabilized in the polar solvent, resulting in an increased energy gap between the ground and excited state. This is in contrast to a positive solvatochromic effect, where the excited state is more energetically favored in the polar solvent. For the CARDIPYs, it appears that the hypsochromic shift with polarity is related to the presence of the positive charge in the ground state.

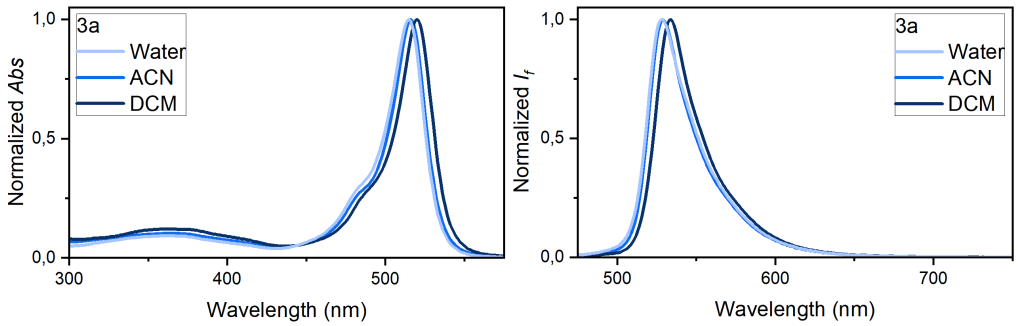

Figure 4.6: Stacked absorption (left) and emission (right) spectra of **3a** to visualize the effect of solvent polarity on λ_{abs} and λ_{em}.

Generally, with decreasing polarity, the Stokes shifts between the compounds tend to decrease, and the fluorescence quantum yields increase (Table 4.3). However, for certain compounds, there is a decrease in fluorescence quantum yield in ACN. The reason for this is unknown, but it could be due to the formation of aggregation or degradation products.

Table 4.3: Steady-state maxima, fluorescence quantum yields, and Stokes shifts of **1a**, **2a**, and **3a** by solvent.

	Solvent	λ_{abs} [nm]	λ_{exc} [nm]	λ_{em} [nm]	Φ_F [%]	$\Delta\nu$ [cm^{-1}]
1a	Water	495	494	513	0,59	709
	ACN	495	494	512	0,64	671
	DCM	499	497	514	1,3	585
2a	Water	493	493	506	4,6	521
	ACN	494	494	506	2,4	480
	DCM	497	497	509	5,4	474
3a	Water	515	517	529	14	514
	ACN	516	518	528	12	476
	DCM	520	525	534	13	504

4.2 Removal of the Aromatic Substituent at the *Meso* Position

The absorption and emission spectra of the compounds without aromatic substitution at the *meso* position (**2f** and **3f**) are drastically blue-shifted from **2a-e** and

3a-e, respectively. This is due to the smaller area of π-conjugation. The emission peak is considerably broad, as can be seen in Figure 4.7, and the Stokes shifts are among the largest of all the compounds (720-856 cm^{-1}). The replacement of the rotating aromatic group with a simple methyl group drastically increases the fluorescence quantum yield. This is a result of decreasing the rate of the nonemissive relaxation pathways associated with the torsion of the phenyl group.

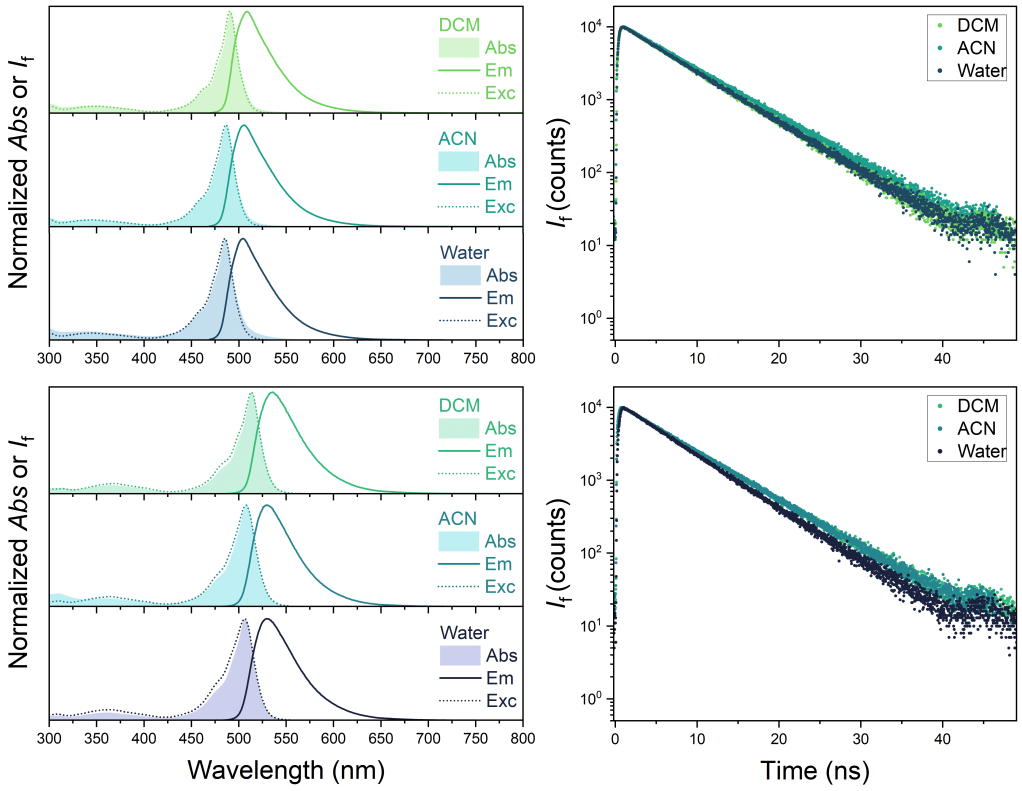

Figure 4.7: Top: Steady-state spectra (left) and fluorescence decays (right) of **2f** by solvent. Bottom: Steady-state spectra (left) and fluorescence decays (right) of **3f** by solvent.

In parallel, the fluorescence lifetimes are long (5,9 to 6,7 ns), and fit well to monoexponential decays (Table 4.4). Without having the π-density bridged by a rotational junction, the molecules are able to stay in the excited state for a longer duration. The monoexponential decay patterns indicate a lack of aggregation upon the removal of the aromatic group at the *meso*-position. The aggregation observed in the other compounds is likely a result of favored intermolecular interactions between the aromatic substituents, such as dipole-dipole interactions. For **2f** and **3f**, the cationic character has more of an influence around the entire molecule, resulting in the favoring of interactions with the solvent.

Table 4.4: Steady-state maxima, fluorescence quantum yields, lifetime fit parameters, and emissive and nonradiative rate constants of **2f** and **3f** by solvent.

	Solvent	λ_{abs} [nm]	λ_{exc} [nm]	λ_{em} [nm]	Φ_F [%]	τ_F [ns]	χ^2	k_F [10^8 s^{-1}]	k_{nr} [10^7 s^{-1}]
2f	Water	486	485	504	78	6,3	1,02	1,2	3,5
	ACN	487	486	506	87	6,7	1,11	1,3	1,9
	DCM	491	490	509	89	6,2	1,11	1,4	1,8
3f	Water	507	506	530	63	5,9	1,09	1,1	6,3
	ACN	508	507	530	44	6,5	1,05	0,7	8,6
	DCM	514	513	536	69	6,5	1,02	1,1	4,8

The lack of influence from a *meso*-position aromatic group in **2f** and **3f** gives an interesting perspective on the effects associated with backbone-substitution patterns. Apparent from the data in Table 4.4, adding the ethyl groups to the CARDIPY core is disadvantageous to the fluorescence quantum yield. The reason for this is not entirely clear.

The solvatochromic effects remain consistent in the absence of the aromatic substituent. By extension of this, there is a considerable increase in the fluorescence quantum yield with decreasing polarity, particularly in **2f**. The highest fluorecence quantum yield in this work was observed from compound **2f** in DCM (89%). From water to DCM, the fluorescence quantum yields of **2f** and **3f** increase from 78% to 89% and 63% to 69%, respectively. This aligns with less favor in interactions with the solvent. For **2f**, the decreased interaction with the solvent is illustrated by a slight increase in the rate of fluorescence with decreasing polarity, and a corresponding decrease in the nonradiative rate constant. With the exception of ACN, the nonradiative rate constant of **3f** also decreases with polarity. However, it is ultimately higher than that of **2f**. Conversely, the rate of fluorescence is not subject to change. In ACN, the absorption spectrum of **3f** degraded quite rapidly over the course of the experiment. A peak grew in at around 310 nm (Figure 4.7), indicating what could be some specific nonemissive aggregate species, or more likely, a degradation product. As a result of this, there is error associated with the strikingly low fluorescence quantum yield of **3f** in ACN.

4.3 Modification of the Aromatic Substituent at the *Meso* Position

Unique photophysical properties can be attained in CARDIPY derivatives due to their facile structure-property tuning. This section serves to discuss the effects of various substitutions at the *para*-position of the *meso*-aromatic group.

4.3.1 Methyl Group

In theory, the addition of a methyl group to the aromatic substituent should induce a slight electron-donating effect toward the CARDIPY core, resulting in an increase in the fluorescence quantum yield. Because of this, electronic effects from the methyl

group were ascribed as the sole reason for the increased fluorescence quantum yields in **1b** (0,72%) and **2b** (11%) when compared to **1a** (0,59%) and **2a** (4,6%), respectively. Doubts arose, however, when the fluorescence quantum yield of **3b** (7,1%) was observed at around half of that of **3a** (14%).

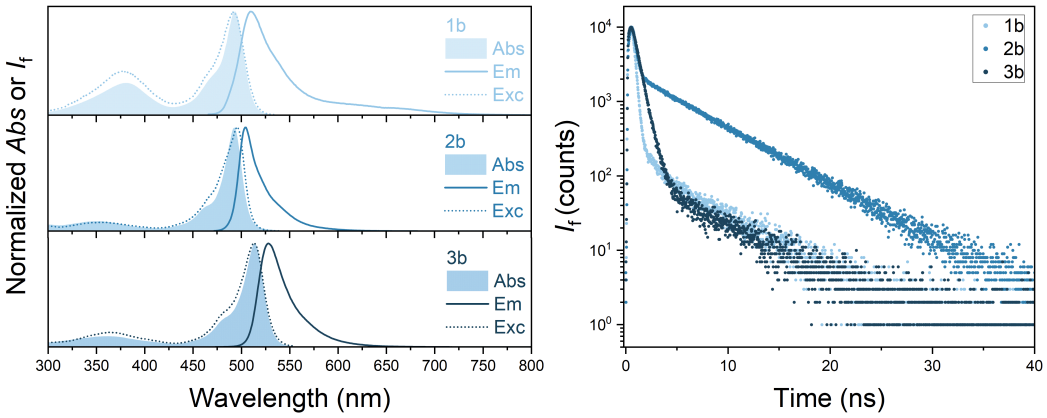

Figure 4.8: Steady-state spectra (left) and fluorescence decays (right) of **1b**, **2b**, and **3b** in aqueous solution.

To understand the differences in fluorescence quantum yield between many of the presented compounds, one must consider the aggregation properties along with the effects of the various substitution patterns. Between **1a** and **1b**, the fluorescence quantum yield increases from 0,59% to 0,72%, but the long-lived lifetime contribution is more than doubled. It can be assumed that a great deal of the signal is related to the formation of potentially emissive aggregates. This could also explain the increase in fluorescence quantum yield between **2a** to **2b** from 4,6% to 11%. As shown in Figure 4.8, the majority (80%) of the decay of **2b** was represented by the long-lived component. Similar behavior was seen throughout all of the solvents (Table 4.5). This could explain the lower energies of the excitation maxima in comparison to the absorption maxima.

Table 4.5: Steady-state maxima, fluorescence quantum yields, and lifetime fit parameters of **1b**, **2b**, and **3b** by solvent.

	Cpd.	λ_{abs} [nm]	λ_{exc} [nm]	λ_{em} [nm]	Φ_F [%]	τ_1 [ns]	τ_2 [ns]	%$_1$	%$_2$	χ^2
Water	1b	494	491	510	0,72	0,2	4,6	87	13	1,02
	2b	493	496	504	11	0,3	5,6	29	71	1,08
	3b	514	512	528	7,1	0,6	5,1	95	5,0	1,00
ACN	1b	494	492	511	0,10	0,4	4,6	91	9,0	1,00
	2b	494	497	505	6,3	0,1	5,7	20	80	1,11
	3b	515	515	529	4,6	0,4	4,8	93	7,0	1,00
DCM	1b	498	495	511	1,9	0,9	2,1	90	10	1,08
	2b	496	502	509	7,4	0,2	5,4	43	57	1,00
	3b	519	519	531	8,4	0,6	4,7	96	4,0	1,00

4.3.2 Fluorine Effect

Bioavailablity is a recurring theme in this work. The hydrophilic nature of the CARDIPYs gives them potential in bioimaging. In the context of drug discovery, metabolic stability is an important factor determining bioavailability. Complications often arise from enzymes in the liver, particularly cytochrome P450[27], which oxidize lipophilic compounds. An avoidance strategy for this involves tuning the polarity by substituting fluorine atoms on the metabolically labile site[28].

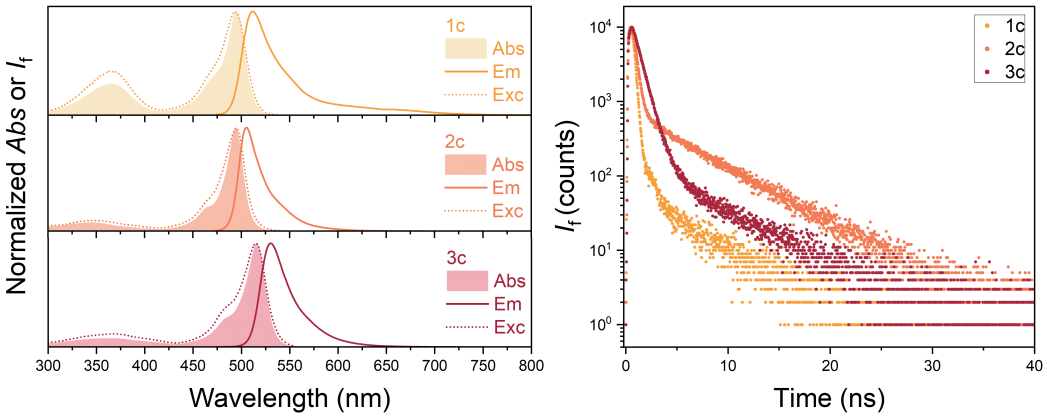

Figure 4.9: Steady-state spectra (left) and fluorescence decays (right) of **1c**, **2c**, and **3c** in aqueous solution.

Despite its electron-withdrawing character, substituting with fluorine resulted in fluorescence quantum yields comparable to the those of the electron-neutral modifiers. The decays of **1c** and **3c** had especially low contribution from the aggregate species in all solvents (3-8%), highlighting effects of solvent and backbone crowding (Table 4.6). The aggregate component contributed more in **2c**, being as high as 37% in water (Figure 4.9), but the effect was not so drastic that the fluorescence quantum yield was higher than that of **3c**. In BODIPY analogues of **2a** and **2c**, substituting with a fluorine atom has led to a similar increase in fluorescence quantum yield[29].

Table 4.6: Steady-state maxima, fluorescence quantum yields, and lifetime fit parameters of **1c**, **2c**, and **3c** by solvent.

	Cpd.	λ_{abs} [nm]	λ_{exc} [nm]	λ_{em} [nm]	Φ_F [%]	τ_1 [ns]	τ_2 [ns]	$\%_1$	$\%_2$	χ^2
Water	1c	495	494	512	0,68	0,2	3,1	94	6,0	1,10
	2c	495	495	508	7,4	0,3	5,5	63	37	1,05
	3c	516	515	528	8,8	0,8	5,2	92	8,0	1,00
ACN	1c	495	494	513	0,74	0,4	4,3	97	3,0	1,00
	2c	496	496	506	4,0	0,2	5,3	87	13	1,03
	3c	517	517	531	5,7	0,5	5,6	93	7,0	1,08
DCM	1c	500	498	514	1,3	0,7	3,5	97	3,0	1,11
	2c	499	499	509	6,8	0,3	5,2	68	32	1,00
	3c	522	521	534	10	0,9	5,2	94	6,0	1,02

4.3.3 Methoxy Group

Substitution with a methoxy group gave compound **1d** a unique absorption profile in that there was considerable signal overlapping with the $S_0 \rightarrow S_1$ peak toward shorter wavelengths. This signal was well-reflected in the emission spectrum, as well as the excitation spectrum (Figure 4.10).

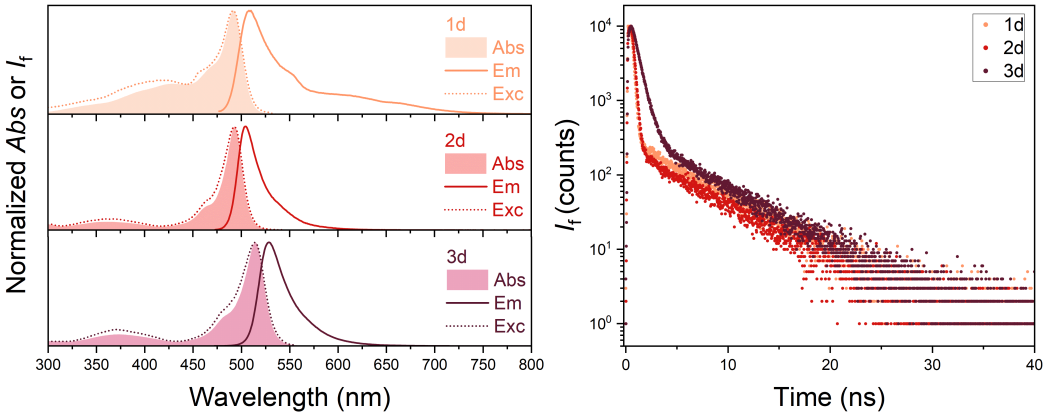

Figure 4.10: Steady-state spectra (left) and fluorescence decays (right) of **1d**, **2d**, and **3d** in aqueous solution.

The fluorescence signal was among the lowest in compounds **1d**, **2d**, and **3d**. Specifically, the lowest fluorescence quantum yield in water belonged to **1d**. It is worth mentioning, however, that the effects from the backbone substituents were able to maintain the fluorescence quantum yields of **2d** and **3d** within one order of magnitude from **2a-c** and **3a-c**, respectively.

Table 4.7: Steady-state maxima, fluorescence quantum yields, and lifetime fit parameters of **1d**, **2d**, and **3d** by solvent.

	Cpd.	λ_{abs} [nm]	λ_{exc} [nm]	λ_{em} [nm]	Φ_F [%]	τ_1 [ns]	τ_2 [ns]	%$_1$	%$_2$	χ^2
Water	1d	492	490	508	0,10	0,1	5,6	73	27	1,00
	2d	493	493	505	2,4	0,2	5,4	83	17	1,00
	3d	514	514	528	7,5	0,6	5,3	82	18	1,00
ACN	1d	492	491	510	0,20	0,2	5,1	94	6,0	1,25
	2d	494	494	505	2,1	0,2	5,5	77	23	1,00
	3d	515	516	528	4,2	0,3	5,4	83	17	1,00
DCM	1d	496	495	515	1,0	0,7	2,0	84	16	1,00
	2d	497	496	507	3,8	0,2	4,9	89	11	1,00
	3d	519	519	531	6,4	0,6	5,3	85	15	1,03

From the lifetime measurement, it could be seen that the aggregates did not contribute too much to the fluorescence signal at the emission maximum (Table 4.7). However, the absorption and emission spectra for **1d** suggest profound aggregation. Importantly, lifetime measurements are not dependent on concentration, nor will the fluorescence decay at a single wavelength determine the nature of the aggregates. It

is more than probable that **1d** is considerably prone to aggregation, but the emission bands of the aggregates do not overlap much with the emission maximum.

4.3.4 Nitro Group

Nitro groups have a well-known quenching effect on fluorescence, complications from which are repeatedly acknowledged in BODIPY reports[30][31][32]. Expectedly, nitro-group substitution in the CARDIPYs resulted in the overall worst fluorescence signal.

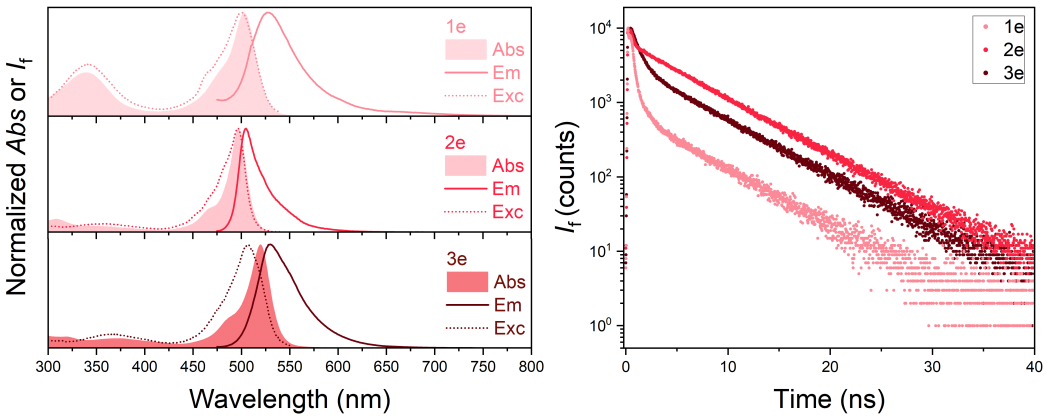

Figure 4.11: Steady-state spectra (left) and fluorescence decays (right) of **1e**, **2e**, and **3e** in aqueous solution.

As shown in Figure 4.11, contribution from emissive aggregates in the decay profiles was very high (42-70% in aqueous solution). The nitro-group quenching effect was strong enough that additional alkyl substituents to the CARDIPY core could not increase the fluorescence quantum yield to over 1% in water (Table 4.8).

Table 4.8: Steady-state maxima, fluorescence quantum yields, and lifetime fit parameters of **1e**, **2e**, and **3e** by solvent.

	Cpd.	λ_{abs} [nm]	λ_{exc} [nm]	λ_{em} [nm]	Φ_F [%]	τ_1 [ns]	τ_2 [ns]	$\%_1$	$\%_2$	χ^2
Water	1e	503	501	524	0,16	0,3	5,1	58	42	1,75
	2e	496	497	505	0,65	0,1	5,7	7,0	93	1,04
	3e	520	n.d.	530	0,95	0,7	5,7	30	70	1,14
ACN	1e	503	501	530	n.d.	0,1	5,2	39	61	1,20
	2e	499	497	508	0,96	0,1	5,6	64	36	1,00
	3e	521	519	538	1,5	0,2	5,9	56	44	1,09
DCM	1e	509	n.d.	532	0,19	n.d.	n.d.	n.d.	n.d.	n.d.
	2e	502	501	512	2,1	0,2	5,1	82	18	1,00
	3e	526	524	541	4,3	0,3	5,4	84	16	1,21

Complications associated with **1e** arise mostly from its solubility problems within the given solvents, especially in DCM, where it is nearly insoluble. The lifetime measurements in ACN and water would not appropriately fit to a biexponential decay.

Instead, a triexponential expression was needed to describe the decay sufficiently well. When characterizing the fluorescence behavior of nearly nonemissive compounds, one must consider the influence of impurities such as aggregates, synthetic contaminants, and decomposition products.

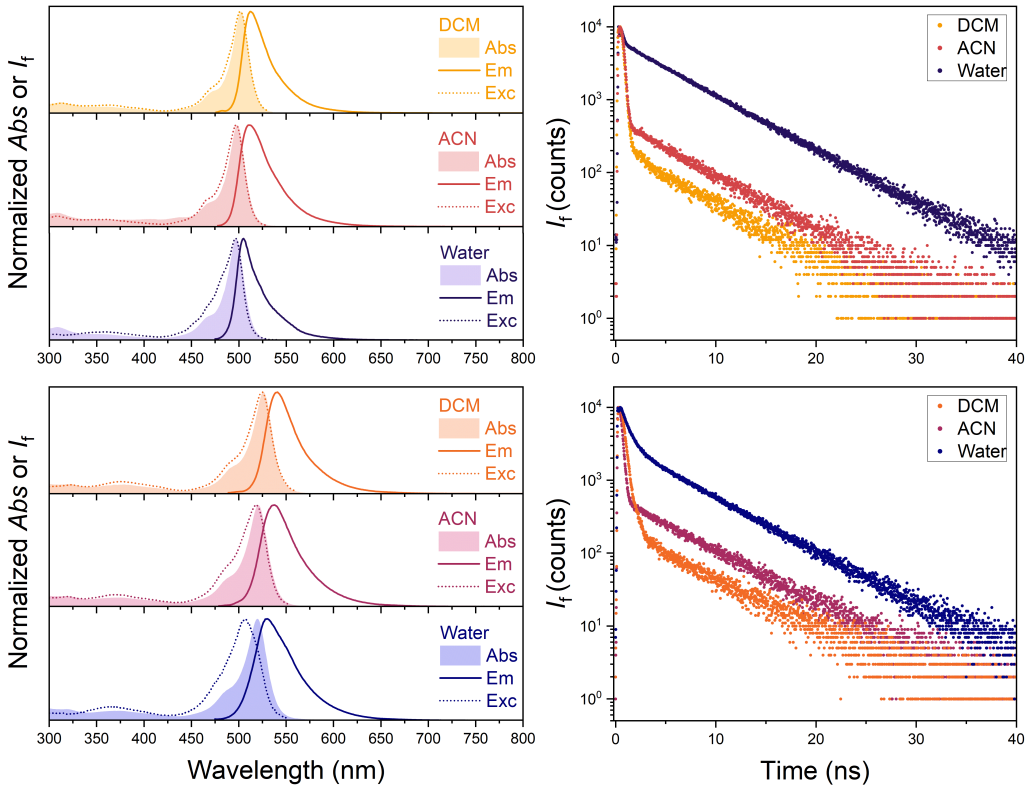

Figure 4.12: Top: Steady-state spectra (left) and fluorescence decays (right) of **2e** by solvent. Bottom: Steady-state spectra (left) and fluorescence decays (right) of **3e** by solvent.

For **2e** and **3e**, emission from aggregate species steeply increased with solvent polarity (Figure 4.12). In water, the excitation maximum of **3e** in monomer form could not be observed due to the heavy overlap with that of the aggregates. The monomer form of **2e** is even more incompatible in water, with its component only contributing to 7% of the decay fitting. However, the excitation maximum of the monomer could be detected, likely due to its more narrow spectra.

4.4 Molecular Rotors

For compounds **1a-e**, the absence of the alkyl substitution at the backbone heavily decreases the energy barrier associated with the rotation of the phenyl group about its bond. Like many BODIPY derivatives, these compounds fall under the category of molecular rotors. It is important to note that free, unrestricted rotation is unlikely, as there still exists steric hindrance between the backbone and the phenyl group. This was demonstrated by the increased bond angle bridging the aromatic group to the backbone in the DFT-optimized structures. For molecular rotors, the fluorescence intensity varies with the competing processes of fluorescence and non-radiative relaxation caused by intramolecular rotation[33]. The emissive properties of molecular rotors are sensitive to their microenvironments, where friction blocks the non-radiative decay channels associated with rotation[34].

4.4.1 Solvent Effects

Without any influence from backbone crowding, the steady-state spectra and fluorescence lifetime measurements of **1a** through **1e** were a good representation on the effect of aromatic group modification on each compound's behavior in DCM and ACN (Figure 4.13).

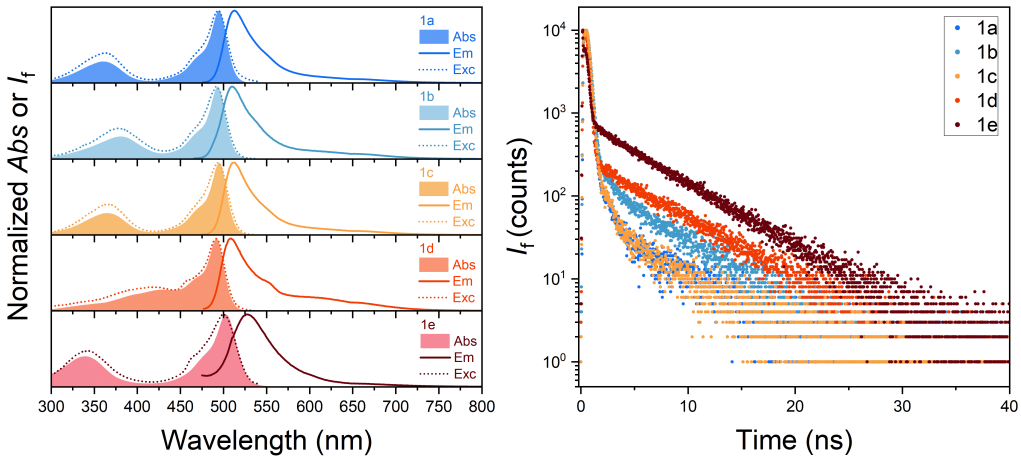

Figure 4.13: Steady-state spectra (left) and fluorescence decays (right) of **1a-1e** in aqueous solution.

Compounds **1a**, **1b**, and **1c** behave similarly when polarity is decreased. In DCM, the absorption and emission spectra are noticeably blue-shifted from those in aqueous solution. In acetonitrile, there is additional broadening of the emission spectra towards the higher wavelengths, which can be seen in Figure 4.14. The reason for this is not entirely known. The absorption and emission behaviors of **1d** and **1e** are particularly sensitive to solvent. This effect is most pronounced for **1e**, whose emission signal was so indiscernible from the noise such that its fluorescence quantum yield in DCM has been excluded.

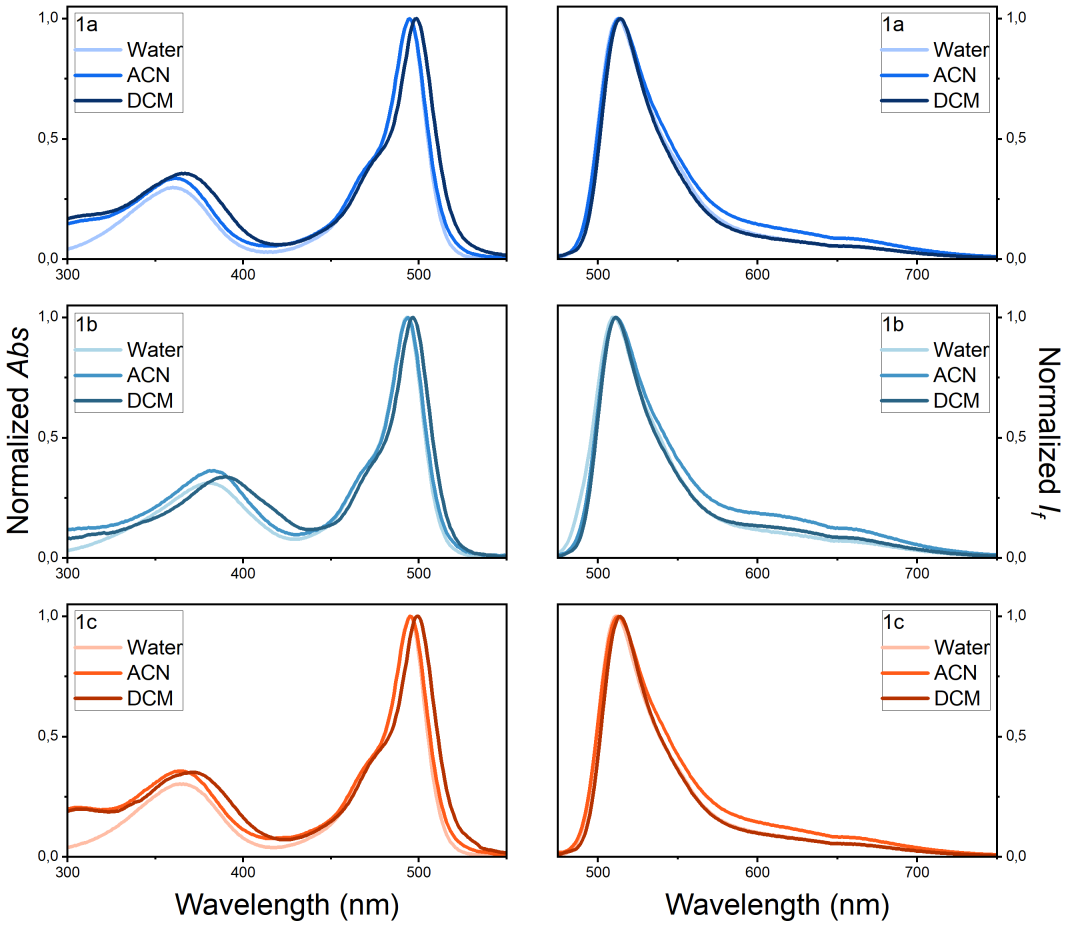

Figure 4.14: Stacked absorption (left) and emission (right) spectra of **1a**, **1b**, and **1c** to visualize the effect of solvent on λ_{abs} and λ_{abs}.

In DCM, the emission spectrum of **1d** experienced intense broadening, but the decay profile retained its high contribution from the short-lived component (Figure 4.15). This behavior has been observed in the formation of excimers[35]. Increasing the polarity induces the growth of an absorption band near 305 nm. In DCM, this band is not reflected in the excitation spectrum. This could be from the formation of a nonemissive aggregate, or a degradation product. In ACN, it is unknown why there is increased intensity in the excitation spectrum within this region.

Table 4.9: Steady-state maxima, fluorescence quantum yields, and lifetime fit parameters of **1d** by solvent.

	Solvent	λ_{abs} [nm]	λ_{exc} [nm]	λ_{em} [nm]	Φ_F [%]	τ_1 [ns]	τ_2 [ns]	$\%_1$	$\%_2$	χ^2
1d	Water	492	490	508	0,10	0,1	5,6	73	27	1,00
	ACN	492	491	510	0,20	0,2	5,1	94	6,0	1,25
	DCM	496	495	515	1,0	0,7	2,0	84	16	1,00

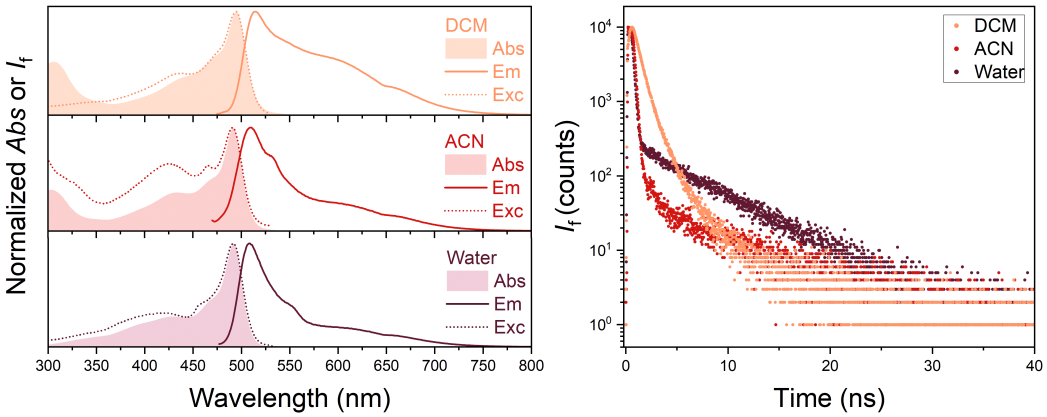

Figure 4.15: Steady-state spectra (left) and fluorescence decays (right) of **1d** by solvent.

4.4.2 Viscosity Dependence

Viscosity is a key factor in determining the flow in any fluid process. Commercial viscometers provide a simple way to measure this parameter, but their scope is limited to the macroscopic scale, where viscosity data is represented as an average. A recurring problem within many engineering applications is the development of methods to measure local viscosity at the small scale[36]. For confined fluids under high pressure, lifetime measurements of viscosity-sensitive dyes have led to success in viscosity probing and mapping[37]. In microfluidic technologies, fluorescent molecular rotors offer a novel technique through fluorescence microscopy to map flow as a measure of local microviscosity[38].

In 2008, Kuimova *et al.* demonstrated in live cells that lifetime-based imaging could also be used to map intracellular viscosity[39]. Since then, a multitude of studies have implemented BODIPY-based molecular rotors for use in viscosity probing and mapping. Among the most common is BODIPY C_{10}[40], which has been used to measure viscosity in plasma membranes[41] and lipid bilayers[42][43], and map the oxidation in organic aerosols[44]. BODIPY C_{10} and similar compounds stand as the base to improve upon when a specific application is necessary[18]. Several reports exist on the design of BODIPY molecular rotors that can localize within a specific organelle, such as the mitochondria[45] and the endoplasmic reticulum membrane[46].

In relation to biological systems, viscosity plays a vital role in diffusion-mediated processes, including the distribution of metabolites, intracellular transport, and substance-signalling[47]. This relationship links intracellular viscosity to cellular functions such as autophagy[48], apoptosis[49], and ferroptosis[50]. Diabetes[51] and neurodegenerative diseases[52] are speculated to have a direct relation to abnormal viscosity within the mitochondria. Lysosomal storage diseases[53] are caused by the inability of the lysosomes to break down macromolecular substances, resulting in the buildup of waste products[54]. In addition, abnormal viscosity related to lyso-

somal dysfunction is often an indicator for other conditions, such as cardiovascular diseases, inflammation, and cancer[55][56][57].

As a result of their cationic nature, the CARDIPYs have already shown mitochondria and lysosome accumulation[20]. Because of this, compounds **1a-e** could function as viscosity sensors used in the detection of conditions related to mitochondrial and lysosomal dysfunction. Taking inspiration from the literature, we demonstrated the viscosity sensitivities of **1a** in aqueous solution by incorporating glycerin in various fractions.

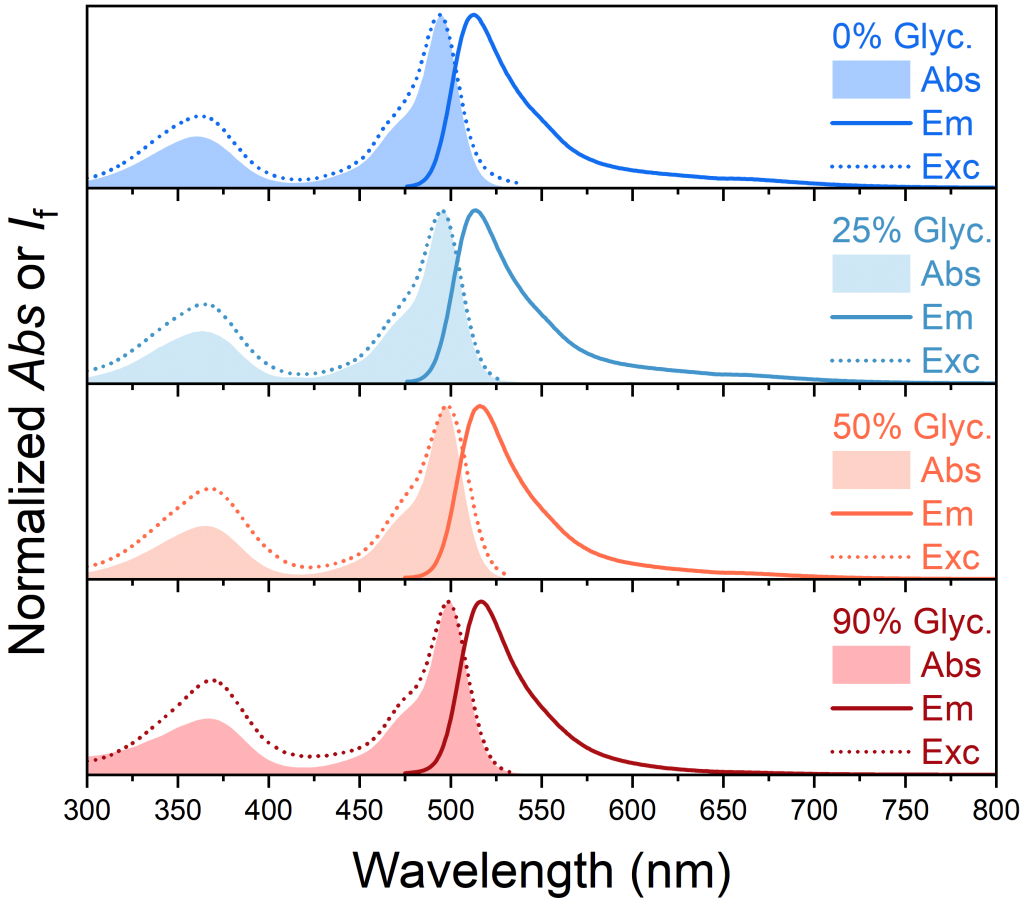

Figure 4.16: Steady-state spectra of **1a** in various glycerin/water solutions.

Expectedly, higher glycerin content is associated with higher fluorescence quantum yields. Increasing the fraction of glycerin to 90% results in a more than ten-fold increase in fluorescence quantum yield (Table 4.10). Adding glycerin also causes a consistent red shift in the absorption and emission maxima. This could be an effect of the increased viscosity, or from the shift in polarity. Emission spectra are also narrowed, specifically from the tail, as shown in Figure 4.16. Likely, this was a result of the added friction to the microenvironment around **1a**

Table 4.10: Steady-state maxima and fluorescence quantum yields of **1a** in various glycerin/water solutions.

$Frac_{glyc.}$	λ_{abs} [nm]	λ_{exc} [nm]	λ_{em} [nm]	Φ_F [%]
0	495	494	513	0,59
0,25	496	495	514	0,83
0,5	497	498	516	1,4
0,9	499	499	517	11

Meaningful time-resolved data could not be obtained in this study. In the presence of glycerin, the intensity of the excitation spectra continuously increased in the 400-450 nm range. This indicates the formation of emissive aggregates. With higher glycerin fractions, this process occurs within an experimental timescale. This unexpected result inspired further studies on the nature of the aggregates formed in different microenvironments.

4.4.3 Aggregation

To study the aggregation patterns in **1a**, absorption spectra in a variety of solvents were recorded over 24 hours in thirty-minute intervals (Figure 4.18). The absorption spectra in water and DCM show very little change over 24 hours. In glycerin, there is an obvious broadening in the absorption spectrum towards shorter wavelengths. The emission is also diminished. This is consistent with the formation of non-emissive H-aggregates.

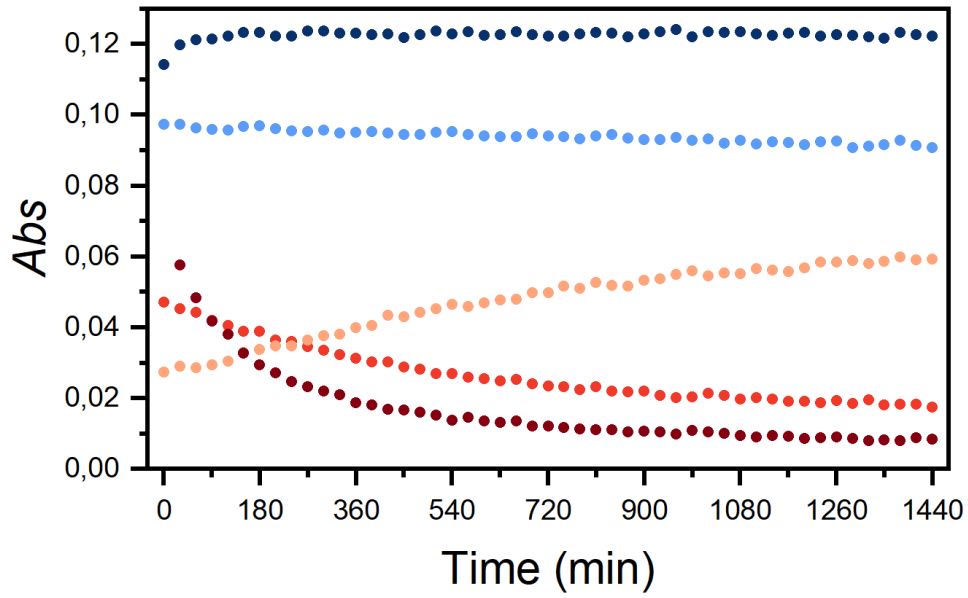

Figure 4.17: Kinetic traces of the prevailing peak of **1a** monomers in DCM (dark blue), water (light blue), ACN (red), 50% (v/v) glycerin/water (orange), and the **1a** H-aggregate peak in 50% (v/v) glycerin/water (yellow).

The kinetic traces in Figure 4.17 show that the growth of the H-aggregate peak (478 nm) and the decay of the monomer peak (497 nm) over time correspond well with one another. It is worth reiterating here that the shoulder of the monomer $S_0 \rightarrow S_1$ peak is likely related to a vibronic species, and only by pure coincidence is it overlapped by the H-aggregate peak.

In acetonitrile, the absorption spectrum is nearly diminished, with the kinetic trace showing a more drastic decay. Near 305 nm, an absorbance band grows in. Similar bands, in parallel with disproportionately low fluorescence quantum yields, have been observed to some extent in most of the compounds. For some compounds, like **2f**, this change is rapid. This complication is likely the result of a decomposition product or a nonemissive aggregate.

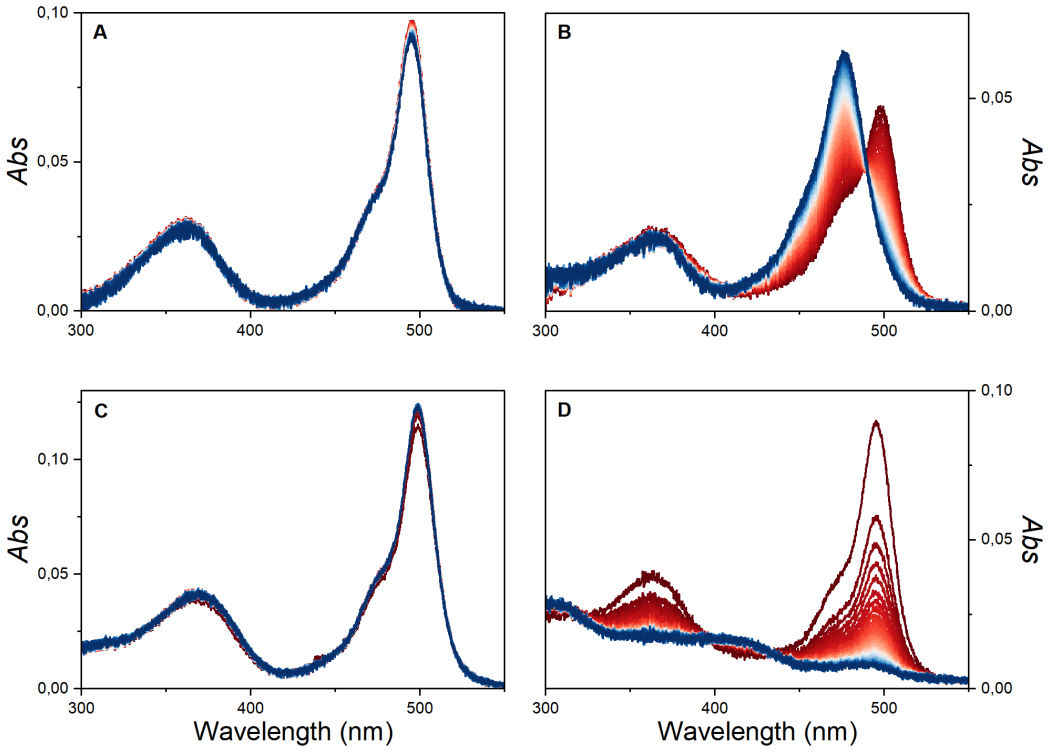

Figure 4.18: Absorption spectra of **1a** recorded over 24 hours in 30-minute intervals in water (A), 50% (v/v) glycerin/water (B), DCM (C), and ACN (D).

5
Conclusion

In the context of bioimaging, CARDIPYs have been developed as a solution to the recurring bioavailability issues associated with the hydrophobicity of many organic dyes. Along with the benefit of their hydrophilic structures is their facile structure-property tuning capability, allowing the synthesis of derivatives with unique photophysical properties.

The steady-state absorption and emission profiles of the compounds in this report show similarities to those of the BODIPYs, whose backbones are analogous in structure. From the absorption spectra a prevailing $S_0 \rightarrow S_1$ peak with a shoulder representing a vibronic structure was identified, with good reflection in the emission spectrum. Towards lower wavelengths, weaker absorption bands corresponding to excitation to higher lying electronic states could be seen in most absorption spectra, with higher absorption for compounds **1a-e**. In regards to the absorption and emission energies, a negative solvatochromic effect was observed in all the compounds, indicating substantial stabilization of the ground state in polar solvents.

Several factors influenced the fluorescence quantum yields. In the compounds with aromatic substitution at the *meso*-position, the π-conjugation is bridged by a rotational junction. For these compounds, fluorescence is in competition with the non-radiative processes associated with the torsion of the aromatic group. Increasing the number of alkyl groups to the CARDIPY backbone restricts this rotation through steric hindrance and inductive effects on the rigidity. This effect is well-demonstrated in the increasing fluorescence quantum yields between **1d**, **2d**, and **3d**. In **2f** and **3f**, a dramatic increase in fluorescence quantum yield results from the lack of the rotational aromatic group. Interestingly, a decrease in fluorescence quantum yield was noted with the added ethyl-groups in **3f**. It is likely that this was influenced by aggregation, which all around is significantly influencing the fluorescence quantum yields. In the case of **2f** and **3f**, the aggregates are nonemissive. It is believed that the rest of the compounds to some extent formed emissive aggregates, which could be differentiated from the monomer emission in the fluorescence decay patterns. Some compounds were more prone to forming emissive aggregates, which disproportionately increase the fluorescence quantum yield. An illustrating example of this is the fluorescence quantum yield of **2b** which is notably higher than that of **3b** in water and ACN. Similar effects are seen in many of the compounds. Modification by a nitro-group expectedly has a strong quenching fluorescence quenching effect on the monomers, causing very high aggregate contribution to the fluorescence signal.

Compounds **1a-e**, which function as molecular rotors, are particularly sensitive to the surrounding microenvironment. This gives them use as viscosity probes. For **1a** in solutions of water and glycerin, it was shown that the fluorescence quantum yield increased from 0,59 percent in water to 11 percent in 90% glycerin. The formation of emissive aggregates was rapid in glycerin, so representative lifetime measurements were not possible. This inspired kinetic studies of **1a** in various solvents. In DCM and water, there is little-to-no change in the absorption spectrum. In 50% glycerin, the prevailing absorption peak at 497 nm gives way to form a new peak at 478 nm, which is consistent with the formation of non-emissive H-aggregates. In ACN, the absorption spectrum changes dramatically over time, suggesting the degradation of the fluorophore or the formation of several aggregate products.

Considering the few existing reports on CARDIPYs, and the reports involving similar BODIPY compounds, it is reasonable to believe that the CARDIPYs presented in this work could have promising applications in microscopy and similar fields. In engineering applications such as microfluidics, similar BODIPYs have been used to determine flow through viscosity mapping. For bioimaging, they have been used to map the visosity in cells to determine changes related to diffusion-mediated processes, which is useful in medical diagnostics. The hydrophilic and cationic nature of the CARDIPYs could give them use in viscosity mapping in the mitochondria and lysosomes, and by extension in microfluidic technologies employing polar solvents.

Bibliography

[1] Wróbel, D., Dudkowiak, A. and Goc, J. "Fluorescence Spectroscopy in Optoelectronics, Photomedicine, and Investigation of Biomolecular Systems." In: *Reviews in Fluorescence 2008.* Ed. by Geddes, C. D. Cham: Springer New York **2010** pp. 237-275. https://doi.org/10.1007/978-1-4419-1260-2

[2] Lakowicz, J. R. *Principles of Fluorescence Spectroscopy.* Springer Science+Business Media, New York, NY **2006**. https://doi.org/10.1007/978-0-387-46312-4

[3] Šteffeková, Z., Kisková, T., Birková, A., Mareková, M., Kostecká, Z., Bedlovičová, Z., Smrčová, M. "Noninvasive Cancer Diagnostics Using Native Fluorescence Analysis of Biological Fluids." In: *Reviews in Fluorescence 2016.* Ed. by Geddes, C. D. Cham: Springer International Publishing **2017** pp. 185-201. https://doi.org/10.1007/978-3-319-48260-6

[4] Tiwari, V. and Solanki, V. "Fluorescence Studies for Biomolecular Structure and Dynamics." In: *Reviews in Fluorescence 2016.* Ed. by Geddes, C. D. Cham: Springer International Publishing **2017** pp. 319-357. https://doi.org/10.1007/978-3-319-48260-6

[5] Harris, D. C. and Lucy, C. A. *Quantitative Chemical Analysis.* W. H. Freeman and Company **2016**, pp. 432-460.

[6] Walla, P. J. "Fluorescence Microscopy." In: *Modern Biophysical Chemistry.* John Wiley & Sons, Ltd. **2014** pp. 169-182. https://doi.org/10.1002/9783527683505

[7] Steiner, R. F. "Fluorescence Anisotropy: Theory and Applications." In: *Topics in Fluorescence Spectroscopy: Principles.* Ed. by Lakowicz, J. R. Boston, MA: Springer US **2002** pp. 1-52. https://doi.org/10.1007/0-306-47058-6

[8] Cheung, H. C. "Resonance Energy Transfer." In: *Topics in Fluorescence Spectroscopy: Principles.* Ed. by Lakowicz, J. R. Boston, MA: Springer US **2002** pp. 127-176. https://doi.org/10.1007/0-306-47058-6

[9] Eftink, M. R. "Fluorescence Quenching: Theory and Applications." In: *Topics in Fluorescence Spectroscopy: Principles.* Ed. by Lakowicz, J. R. Boston, MA: Springer US **2002** pp. 53-126. https://doi.org/10.1007/0-306-47058-6

[10] Huang, S., Heikal, A. and Webb, W. Two-Photon Fluorescence Spectroscopy and Microscopy of NAD(P)H and Flavoprotein. *Biophysical Journal* **2002** 82(5): 2811-2825. https://doi.org/10.1016/S0006-3495(02)75621-X

[11] Benson, R. C., Meyer, R. A., Zaruba, M. E., and McKhann, G. M. Cellular autofluorescence–is it due to flavins? *Journal of Histochemistry & Cytochemistry* **1979** 27(1): 44-48. https://doi.org/10.1177/27.1.438504

[12] Monici, M. Cell and tissue autofluorescence research and diagnostic applications. *Elsevier, Biotechnology Annual Review* **2005** 11: 227-256. https://doi.org/10.1016/S1387-2656(05)11007-2

[13] Menter, J. M. Temperature dependence of collagen fluorescence. *Photochem Photobiol Sci* **2006** 5: 403-410. https://doi.org/10.1039/b516429j

[14] Robertson, T. A., Bunel, F. and Roberts, M. S. Fluorescein Derivatives in Intravital Fluorescence Imaging. *Cells* **2013** 2(3): 591-606. https://doi.org/10.3390/cells2030591

[15] Brouwer, A. M. Standards for photoluminescence quantum yield measurements in solution (IUPAC Technical Report). *Pure Appl. Chem.* **2011** 83(12): 2213-2228. https://doi.org/10.1351/PAC-REP-10-09-31

[16] Schade, S. Z., Jolley, M. E., Sarauer, B. J. and Simonson, L. G. BODIPY–α-Casein, a pH-Independent Protein Substrate for Protease Assays Using Fluorescence Polarization. *Analytical Biochemistry* **1996** 243(1): 1-7. https://doi.org/10.1351/10.1006/abio.1996.0475

[17] Hu, R., Lager, E., Aguilar-Aguilar, A., Liu, J., Lam, J. W. Y., Sung, H. H. Y., Williams, I. D., Zhong, Y., Wong, K. S., Peña-Cabrera, E. and Tang, B. Z. Twisted Intramolecular Charge Transfer and Aggregation-Induced Emission of BODIPY Derivatives. *The Journal of Physical Chemistry C* **2009** 113, 36; 15845-15853. https://doi.org/10.1021/jp902962h

[18] Maleckaitė, K., Dodonova, J., Toliautas, S., Žilėnaitė, R., Jurgutis, D., Karabanovas, V., Tumkevičius, S., and Vyšniauskas, A. Designing a Red-Emitting Viscosity-Sensitive BODIPY Fluorophore for Intracellular Viscosity Imaging. *Chemistry – A European Journal* **2021** 27(67): 16768-16775. https://doi.org/10.1002/chem.202102743

[19] Donuru, V. R., Zhu, S., Green, S. and Liu, H. Near-infrared emissive BODIPY polymeric and copolymeric dyes. *Polymer* **2010** 51(23): 5359-5368. https://doi.org/10.1016/j.polymer.2010.09.029

[20] Zhang, H., Liu, J., Sun, Y.-Q., Liu, M. and Guo, W. Carbon-Dipyrromethenes: Bright Cationic Fluorescent Dyes and Potential Application in Revealing Cellular Trafficking of Mitochondrial Glutathione Conjugates. *J. Am. Chem. Soc.* **2020** 142: 17069-17078. https://doi.org/10.1021/jacs.0c06916

[21] Koek, J.H., van der Hoef, K., Roodenburg, L., Lugtenburg, J. and Fokkens, R. Synthesis and properties of two pyrromethenium salts; one with a rigid Z-syn structure and another with a rigid E-anti structure. *Recl. Trav. Chim. Pays-Bas* **1991** 110: 41-45. https://doi.org/10.1002/recl.19911100203

[22] Tam, L. K. B., Lo, P.-C., Cheung, P. C. K., Ng, D. K. P. A Tetrazine-Caged Carbon-Dipyrromethene as a Bioorthogonally Activatable Fluorescent Probe. *Chem Asian J.* **2023** 18(17): e202300562. https://doi.org/10.1002/asia.e202300562

[23] Ware, W. R., and Rothman, W. Relative fluorescence quantum yields using an integrating sphere. The quantum yield of 9,10-diphenylanthracene in cyclohexane. *Chemical Physics Letters* **1976** 39(3): 449-453. https://doi.org/10.1016/0009-2614(76)80301-6

[24] Magde, D., Wong, R., and Seybold, P. G. Fluorescence Quantum Yields and Their Relation to Lifetimes of Rhodamine 6G and Fluorescein in Nine

Solvents: Improved Absolute Standards for Quantum Yields. *Photochemistry and Photobiology* **2002** 75(4): 327-334. https://doi.org/10.1562/0031-8655(2002)0750327FQYATR2.0.CO2

[25] Wu, Y., Štefl, M., Olzyńska, A., Hof, M., Yahioglu, G., Yip, P., Casey, D. R., Ces, O., Humpolíčková, J. and Kuimova, M. K. Molecular rheometry: direct determination of viscosity in Lo and Ld lipid phases via fluorescence lifetime imaging. *Phys. Chem. Chem. Phys.* **2013** 15(36): 14986-14993. https://doi.org/10.1039/C3CP51953H

[26] Loudet, A., and Burgess, K. BODIPY Dyes and Their Derivatives: Syntheses and Spectroscopic Properties. *Chemical Reviews* **2007** 107(7): 4891-4932. https://doi.org/10.1021/cr078381n

[27] Patrick, G. L. *An Introduction to Medicinal Chemistry,* 6th ed.; Oxford University Press: New York, NY, 2017, p 100.

[28] Böhm, H.-J., Banner, D., Bendels, S., Kansy, M., and Kuhn, B., Müller, K., Obst-Sander, U., and Stahl, M. Fluorine in Medicinal Chemistry. *ChemBioChem* **2004** 5(5): 637-643. https://doi.org/10.1002/cbic.200301023

[29] Alamiry, M. A. H., Benniston, A. C., Hagon, J., Winstanley, T. P. L., Lemmetyinen, H., and Tkachenko, N. V. The fluorine effect: photophysical properties of borondipyrromethene (bodipy) dyes appended at the meso position with fluorinated aryl groups. *RSC Adv.* **2012** 2(11): 4944-4950. https:doi.org/10.1039/C2RA20219K

[30] Cunha Dias de Rezende, L., Menezes Vaidergorn, M., Biazzotto Moraes, J.C. *et al.* Synthesis, Photophysical Properties and Solvatochromism of Meso-Substituted Tetramethyl BODIPY Dyes. *J Fluoresc.* **2014** 24, 257-266. https://doi.org/10.1007/s10895-013-1293-8

[31] Cui, A., Peng, X., Fan, J., Chen, X., Wu, Y., and Guo, B. Synthesis, spectral properties and photostability of novel boron–dipyrromethene dyes. *Journal of Photochemistry and Photobiology A: Chemistry* **2007** 186(1): 85-92. https://doi.org/10.1016/j.jphotochem.2006.07.015

[32] Pavlopoulos, T. G., Boyer, J. H., Shah, M., Thangaraj, K., and Soong. M.-L. Laser action from 2,6,8-position trisubstituted 1,3,5,7-tetramethylpyrromethene-BF2 complexes: part 1. *Appl. Opt.* **1990** 29(4): 3885-3886. https:doi.org/10.1364/AO.29.003885

[33] Maleckaitė, K., Dodonova, J., Toliautas, S., Žilėnaitė, R., Jurgutis, D., Karabanovas, V., Tumkevičius, S., Vyšniauskas, A. Designing a Red-Emitting Viscosity-Sensitive BODIPY Fluorophore for Intracellular Viscosity Imaging. *Chem. Eur. J.* **2021** 27, 16768. https://doi.org/10.1002/chem.202102743

[34] Lou, Z., Hou, Y., Chen, K., Zhao, J., Ji, S., Zhong, F., Dede, Y., and Dick, B. Different Quenching Effect of Intramolecular Rotation on the Singlet and Triplet Excited States of Bodipy. *The Journal of Physical Chemistry C* **2018** 122(1), 185-193. https://doi.org/10.1021/acs.jpcc.7b10466

[35] Musser, A. J., Rajendran, S. K., Georgiou, K., Gai, L., Grant, R. T., Shen, Z., Cavazzini, M., Ruseckas, A., Turnbull, G. A., Samuel, I. D. W., Clark, J. and Lidzey, D. G. Intermolecular states in organic dye dispersions: excimers vs. aggregates. *J. Mater. Chem. C.* **2017** 5(33): 8380-8389. https://doi.org/10.1039/C7TC02655B

[36] Barnes, H. A. On-line or Process Viscometry – A Review. *Applied Rheology* **1999** 9(3): 102-107. https://doi.org/10.1515/arh-2009-0007

[37] Ponjavic, A., Dench, J., Morgan, N., and Wong, J. S. S. *In situ* viscosity measurement of confined liquids. *RSC Adv.* **2015** 5(121): 99585-99593. https://doi.org/10.1039/C5RA19245E

[38] Nalatamby, D., Gibouin, F., Ordóñez-Hernández, J., Renaudeau, J., Clisson, G., Farfán, N., Lidon, P., and Medina-Gonzalez, Y. Molecular Rotors for In Situ Local Viscosity Mapping in Microfluidic Chips. *Industrial & Engineering Chemistry Research* **2023** 62(32): 12656-12667. https://doi.org/10.1021/acs.iecr.3c01047

[39] Kuimova, M. K., Yahioglu, G., Levitt, J. A. and Suhling, K. Molecular Rotor Measures Viscosity of Live Cells via Fluorescence Lifetime Imaging. *Journal of the American Chemical Society* **2008** 130(21): 6672-6673. https://doi.org/10.1021/ja800570d

[40] Polita, A., Toliautas, S., Žvirblis, R. and Vyšniauskas, A. The effect of solvent polarity and macromolecular crowding on the viscosity sensitivity of a molecular rotor BODIPY-C10. *Phys. Chem. Chem. Phys.* **2020** 22(16): 8296-8303. https://doi.org/10.1039/C9CP06865A

[41] Mika, J. T., Thompson, A. J., Dent, M. R., Brooks, N. J., Michiels, J., Hofkens, J. and Kuimova, M. K. Measuring the Viscosity of the Escherichia coli Plasma Membrane Using Molecular Rotors. *Biophysical Journal* **2016** 111(7): 1528-1540. https://doi.org/10.1016/j.bpj.2016.08.020

[42] Dent, M. R., López-Duarte, I., Dickson, C. J., Geoghegan, N. D., Cooper, J. M., Gould, I. R., Krams, R., Bull, J. A., Brooks, N. J. and Kuimova, M. K. Imaging phase separation in model lipid membranes through the use of BODIPY based molecular rotors. *Phys. Chem. Chem. Phys.* **2015** 17(28): 18393-18402. https://doi.org/10.1039/C5CP01937K

[43] Vyšniauskas, A., Qurashi, M. and Kuimova, M. K. A Molecular Rotor that Measures Dynamic Changes of Lipid Bilayer Viscosity Caused by Oxidative Stress. *Chemistry - A European Journal* **2016** 22(37): 13210-13217. https://doi.org/10.1002/chem.201601925

[44] Athanasiadis, A., Fitzgerals, C., Davidson, N. M., Giorio, C., Botchway, S. W., Ward, A. D., Kalberer, M., Pope, F. D., and Kuimova, M. K. Dynamic viscosity mapping of the oxidation of squalene aerosol particles. *Phys. Chem. Chem. Phys.* **2016** 18(44): 30385-30393. https://doi.org/10.1039/C6CP05674A

[45] Su, D., Teoh, C. L., Gao, N., Xu, Q.-H., and Chang, Y.-T. A Simple BODIPY-Based Viscosity Probe for Imaging of Cellular Viscosity in Live Cells. *Sensors* **2016** 16(9). https://doi.org/10.3390/s16091397

[46] Lee, H., Yang, Z., Wi, Y., Kim, T. W., Verwilst, P., Lee, Y. H., Han, G., Kang, C. and Kim, J. S. BODIPY–Coumarin Conjugate as an Endoplasmic Reticulum Membrane Fluidity Sensor and Its Application to ER Stress Models. *Bioconjugate Chemistry* **2015** 26(12): 2474-2480. https://doi.org/10.1021/acs.bioconjchem.5b00508

[47] Kuimova, M. K., Botchway, S. W., Parker, A. W„ Balaz, M., Collins, H. A., Anderson, H. L., Suhling, K., Ogilby, P. R. Imaging intracellular viscosity of

a single cell during photoinduced cell death. *Nat. Chem.* **2009** 1(1): 69-73. https://doi.org/10.1038/nchem.120.

[48] Ding, S. and Hong, Y. The fluorescence toolbox for visualizing autophagy. *Chem. Soc. Rev.* **2020** 49(22): 8354-8389. https://doi.org/10.1039/D0CS00913J

[49] Hou, M.-X., Liu, L.-Y., Wang, K.-N., Chao, X.-J., Liu, R.-X. and Mao, Z.-W. A molecular rotor sensor for detecting mitochondrial viscosity in apoptotic cells by two-photon fluorescence lifetime imaging. *New J. Chem.* **2020** 44(26): 11342-11348. https://doi.org/10.1039/D0NJ02108C

[50] Dong, B., Song, W., Lu, Y., Sun, Y. and Lin, W. Revealing the Viscosity Changes in Lipid Droplets during Ferroptosis by the Real-Time and In Situ Near-Infrared Imaging. *ACS Sensors* **2021** 6(1): 22-26. https://doi.org/10.1021/acssensors.0c02015

[51] Nadiv, O., Shinitzky, M., Manu, H., Hecht, D., Roberts, Jr, C. T., LeRoith, D. and Zick, Y. Elevated protein tyrosine phosphatase activity and increased membrane viscosity are associated with impaired activation of the insulin receptor kinase in old rats. Biochem. J. **1994** 298(part 2): 443–450. https://doi.org/10.1042/bj2980443

[52] Yang, J., Guo, Y., Pistolozzi, M. and Yan, J. Research progress of multifunctional fluorescent probes for Alzheimer's disease monitoring. *Dyes and Pigments* **2021** 193: 109466. https://doi.org/10.1016/j.dyepig.2021.109466

[53] Futerman, A. H. and van Meer, G. The cell biology of lysosomal storage disorders. *Nat. Rev. Mol. Cell Biol.* **2004** 5: 554-565. https://doi.org/10.1038/nrm1423

[54] Xu, J.-F., Gu, J., Qi, Y.-L., Zhang, M., Chen, J., Li, D.-D., Yang, Y.-S., Lv, P.-C. and Zhu, H.-L. Exploiting novel rotors with auxochromic dynamic motors for monitoring lysosomal viscosity. *Dyes and Pigments* **2021** 186: 108974. https://doi.org/10.1016/j.dyepig.2020.108974

[55] Shen, B., Wang, L. F., Zhi, X. and Qian, Y. Construction of a red emission BODIPY-based probe for tracing lysosomal viscosity changes in culture cells. *Sensors and Actuators B: Chemical* **2020** 304: 127271. https://doi.org/10.1016/j.snb.2019.127271

[56] Wang, L., Xiao, Y., Tian, W. and Deng, L. Activatable Rotor for Quantifying Lysosomal Viscosity in Living Cells. *J. Am. Chem. Soc.* **2013** 135(8): 2903-2906. https://doi.org/10.1021/ja311688g

[57] Yang, X., Zhang, D., Ye, Y. and Zhao, Y. Recent advances in multifunctional probes for viscosity and analytes. *Coordination Chemistry Reviews* **2022** 453: 214336. https://doi.org/j.ccr.2021.214336

A

Appendix 1

A.1 Solvent Choice

Solvent suitability was determined for all the derivatives by monitoring their absorption spectra over time. In water and DCM, all the derivatives showed high thermal stability; no additional features grew into their absorption spectra. In ACN, this was also the case for most derivatives, but some experienced changes indicating what could be degradation or aggregation. For example, within an experimental timescale, the absorption spectra of **2f** and **3f** completely disappeared, giving rise to an unstructured peak in the UV region. DMSO, ethanol, and methanol were considered for this study, but due to rapid degradation of the fluorophores, work was not continued in these solvents.
Some of the CARDIPYs show poor solubility within certain solvents, e.g. toluene, which was considered for this study, but during initial screening no solvation could be observed. Of the three solvents that were deemed suitable, DCM showed the most complications with solubility respective to the collection of CARDIPYs, being the least polar of all the solvents used. Many of the derivatives with more hydrophobic substituents (**2a-b**, **3a**) showed slower solubility in water, sometimes also in ACN. This was also the case for methoxy-substituted derivatives (**2d**, **3d**). CARDIPY **1e** showed the least solubility within the three chosen solvents, being completely insoluble in DCM.

A.2 Complete List of Optical Properties

Table A.1: Steady-state maxima, fluorescence quantum yields, and lifetime fit parameters of all CARDIPY derivatives in aqueous solution.

Cpd.	λ_{abs} [nm]	λ_{exc} [nm]	λ_{em} [nm]	Φ_F	τ_1 [ns]	τ_2 [ns]	%$_1$	%$_2$	χ^2
1a	495	494	513	0,0058	0,2	3,3	94	6,0	1,25
2a	493	493	506	0,046	0,3	3,8	86	14	1,04
3a	515	517	529	0,140	0,7	5,5	44	56	1,11
1b	494	491	510	0,0072	0,2	4,6	87	13	1,02
2b	493	496	504	0,11	0,3	5,6	29	71	1,08
3b	514	512	528	0,071	0,6	5,1	95	5,0	1,00
1c	495	493	512	0,0068	0,2	3,1	94	6,0	1,10
2c	495	495	506	0,074	0,3	5,5	63	37	1,05
3c	516	515	530	0,10	0,8	5,2	92	8,0	1,00
1d	492	490	508	0,0010	0,1	5,6	73	27	1,00
2d	493	493	505	0,024	0,2	5,4	83	17	1,00
3d	514	514	528	0,075	0,6	5,3	82	18	1,00
1e	503	499	524	0,0016	0,3	5,1	58	42	1,75
2e	496	497	505	0,0065	0,1	5,7	7,0	73	1,04
3e	520	n.d.	530	0,0095	0,7	5,7	30	70	1,14
2f	486	485	504	0,78	6,3		1,00		1,02
3f	507	506	530	0,63	5,9		1,00		1,09

Table A.2: Steady-state maxima, fluorescence quantum yields, and lifetime fit parameters of all CARDIPY derivatives in ACN.

Cpd.	λ_{abs} [nm]	λ_{exc} [nm]	λ_{em} [nm]	Φ_F	τ_1 [ns]	τ_2 [ns]	%$_1$	%$_2$	χ^2
1a	495	494	512	0,006	0,3	2,7	97	3,0	1,00
2a	494	494	506	0,024	0,2	3,3	85	15	1,44
3a	516	518	529	0,090	0,4	5,7	35	65	1,03
1b	494	492	511	0,001	0,4	4,6	91	9,0	1,00
2b	494	497	505	0,063	0,1	5,7	20	80	1,11
3b	515	515	529	0,046	0,4	4,8	93	7,0	1,00
1c	495	494	513	0,0074	0,4	4,3	97	3,0	1,00
2c	496	496	506	0,040	0,2	5,3	87	13	1,03
3c	517	517	531	0,057	0,5	5,6	93	7,0	1,08
1d	492	491	510	0,0020	0,2	5,1	94	6,0	1,25
2d	494	494	505	0,021	0,2	5,5	77	23	1,00
3d	515	516	528	0,042	0,3	5,4	83	17	1,00
1e	503	501	530	n.d.	0,1	5,2	39	61	1,20
2e	499	497	508	0,0096	0,1	5,6	64	36	1,00
3e	521	519	538	0,015	0,2	5,9	56	44	1,09
2f	487	486	506	0,87	6,7		1,00		1,11
3f	508	507	530	0,44	6,5		1,00		1,05

Table A.3: Steady-state maxima, fluorescence quantum yields, and lifetime fit parameters of all CARDIPY derivatives in DCM.

Cpd.	λ_{abs} [nm]	λ_{exc} [nm]	λ_{em} [nm]	Φ_F	τ_1 [ns]	τ_2 [ns]	%$_1$	%$_2$	χ^2
1a	499	497	514	0,013	0,7	3,3	88	12	1,28
2a	497	497	509	0,054	0,3	3,4	92	8,0	1,00
3a	520	525	534	0,13	0,8	5,7	56	44	1,00
1b	498	495	511	0,019	0,9	2,1	90	10	1,08
2b	496	502	509	0,074	0,2	5,4	43	57	1,00
3b	519	519	531	0,084	0,6	4,7	96	4,0	1,00
1c	500	498	514	0,013	0,7	3,5	97	3,0	1,11
2c	499	499	509	0,068	0,3	5,2	68	32	1,00
3c	522	521	534	0,10	0,9	5,2	94	6,0	1,02
1d	496	495	515	0,010	0,7	2,0	84	16	1,00
2d	497	496	507	0,038	0,2	4,9	89	11	1,00
3d	519	519	531	0,064	0,6	5,3	85	15	1,03
1e	509	506	532	0,0019	n.d.	n.d.	n.d.	n.d.	n.d.
2e	502	501	512	0,021	0,2	5,1	82	18	1,00
3e	526	524	541	0,043	0,3	5,4	84	16	1,21
2f	491	490	509	0,89	6,2		1,0		1,11
3f	514	513	536	0,69	6,5		1,0		1,02

DEPARTMENT OF CHEMISTRY AND CHEMICAL ENGINEERING
CHALMERS UNIVERSITY OF TECHNOLOGY
Gothenburg, Sweden
www.chalmers.se

CHALMERS
UNIVERSITY OF TECHNOLOGY